Optimal Control in an Open Quantum System: Selecting DNP Pathways in an Electron-Nuclear System

by

Sarah Sheldon

Submitted to the Department of Nuclear Science and Engineering
in partial fulfillment of the requirements for the degree of

Doctor of Philosophy in Nuclear Science and Engineering

at the

MASSACHUSETTS INSTITUTE OF TECHNOLOGY

June 2013

Author ....
Department of Nuclear Science and Engineering
June, 2013

Certified by ....
David G. Cory
Professor
Thesis Supervisor

Read by ....
Paola Cappellaro
Assistant Professor

Accepted by ....
Mujid S. Kazimi
Chair, Department Committee on Graduate Students
TEPCO Professor of Nuclear Engineering

Optimal Control in an Open Quantum System: Selecting DNP Pathways in an Electron-Nuclear System

by

Sarah Sheldon

Submitted to the Department of Nuclear Science and Engineering
on June, 2013, in partial fulfillment of the
requirements for the degree of
Doctor of Philosophy in Nuclear Science and Engineering

Abstract

There is much interest in improving quantum control techniques for the purposes of quantum information processing. High fidelity control is necessary for the future of quantum computing. Optimal control theory has been used successfully to numerically optimize control sequences for spin-based systems. Previous control pulse finding efforts have primarily optimized pulses to a desired unitary control. Non-unitary dynamics are unavoidable in quantum systems, and, to improve current control techniques, interactions with the environment and stochastic noise processes must be incorporated into pulse design. We present here a method of pulse optimization that includes decoherence.

This thesis discusses a particular example of engineering control for an open quantum system: selecting transfer pathways in dynamic nuclear polarization. Dynamic nuclear polarization (DNP) is a method of increasing the nuclear spin magnetization in a nuclear magnetic resonance experiment. DNP works by transferring polarization from a coupled electron spin. In solid state systems, however, there are multiple pathways through which polarization can be transferred. Excitation of more than one pathway can prevent the nuclear spin from achieving the maximum possible polarization. It is demonstrated in this thesis that optimal control theory (OCT) can be used to design pulses which will select one pathway and suppress the others. The pulses were found considering the open quantum system dynamics.

This work includes an algorithm for generating noise realizations from a spectral density function. Future efforts to engineer high-fidelity control could use this method to incorporate stochastic noise in the pulse finding process.

Thesis Supervisor: David G. Cory
Title: Professor

Acknowledgments

This thesis is the product of a long search for a signal, a busted amplifier, and the support of many friends, family, and colleagues. The pursuit of my PhD has been an rewarding and challenging experience, alternatingly frustrating and inspiring. I did not do this alone but only with the help of many people around me.

I would first like to acknowledge my advisor David Cory. From him I have learned not only a great deal of NMR and quantum information, but also what it means to be a good experimentalist and a good scientist. He has challenged me to ask questions and to demand thorough analysis of the answers.

Thank you also to Chandrasekhar Ramanathan, a patient teacher, for many insightful discussions, and to Paola Cappellaro and Bilge Yildiz for given me the opportunity to teach as well.

I was also fortunate to be surrounded by so many enthusiastic students at MIT and Waterloo. The members of Cory group have become my teachers and my friends, and I hope to cross paths with many of them in the future both in science and in life. I am grateful to have navigated the Boston-Waterloo migration together with Troy Borneman and Kevin Krsulich, and I am much obliged to those who have contributed directly to work here, particulary Chris Granade, Holger Haas, and Hamid Mohebbi.

My most sincere gratitude goes to Pat Gumann, who showed me how to use a lathe, proofread every word of this thesis, and encouraged me endlessly.

Finally, I am forever thankful for my family and for their constant love, occasional worry, and obvious pride.

Contents

List of Figures

Chapter 1

Introduction

Spin based systems are one candidate for a quantum computing architecture [88, 87, 48]. Coupled electron-nuclear solid state systems are particularly appealing as quantum processors. Nuclear spins may serve as a quantum memory due to their long coherence times and weak interactions with their environment[42, 84], while electron spins allow faster initialization and gate operations. Magnetic resonance systems and methods have permitted the experimental examination of quantum information algorthims [20, 41, 51], error correction[22], quantum metrology[15], and control techniques [30, 79, 36].

Nuclear magnetic resonance has long served as a testbed for QIP [23, 1]. In magnetic resonance spectroscopy, an ensemble of spins are aligned with a large external magnetic field and controlled by a RF (for NMR) or microwave (for electron spin resonance) field. We cannot perform projective measurements in NMR or ESR as the coupling between the spin system and the detection circuit is too weak. We must use averages over many spins instead and rely on expectation value measurements. Thus we have a highly mixed state with some small deviation from identity, and that deviation, or polarization, is the actual observable. It is desirable to increase this purity of this state. This improves sensitivity and reduces the entropy in the system, concepts which can extend beyond NMR to other qubit systems.

This thesis will discuss one method of enhancing the nuclear spin polarization: dynamic nuclear polarization. DNP effectively transfers the electron magnetization to the nucleus in a coupled electron-nuclear system. This results in an enhancement of the nuclear spin signal as the electron magnetic moment is more than two orders of magnitude greater than the largest nuclear magnetic moment. The transfer of polarization in DNP can occur through several pathways in the electron-nucleus system. Relaxation plays an important role in this process, and thus the description of DNP requires an open quantum system treatment.

While DNP is well-used and well-studied in NMR, it is an interesting problem in a wider context. We can consider the different pathways of DNP to be various information pathways in a more general open quantum framework. Often one may want to select a particular pathway without exciting other unwanted transitions. For DNP, as we will show in later chapters, this can provide a greater nuclear enhancement. When the spin transitions are close or there is an overlap between the desired excitation frequencies and other, unwanted transitions in the system, more sophisticated control techniques are required. In this work we use optimal control theory to find control sequences that generate the desired open quantum dynamics and select one DNP pathway.

OCT and DNP are both valuable resources in magnetic resonance spectroscopy, outside of the scope of QIP. The use of nuclear spins to store information is highly relevant for medical imaging. Nuclear spins are of course used already for traditional MRI, and one avenue of improvement in this field is to develop highly polarized tracers with long coherence times that can be injected and imaged in vivo [6]. Sensitivity and control still limit the usefulness of these techniques. DNP with OCT could provide greater enhancements in these settings as well.

This thesis discusses open quantum system dynamics and describes the methods of dynamic nuclear polarization and optimal control theory in the first few chapters. We then show in Chapter 5 how we developed microwave pulses and simulated these control sequences for performing DNP in a specific electron-nuclear system, malonic acid. Chapter 6 outlines the experimental setup and presents the results of performing DNP with OCT pulses. The final chapter is a self-contained discussion of an algorithm we propose for generating noise realizations of Gaussian processes with a given spectral density. We begin by presenting the complete Hamiltonian for the electron-nuclear system and describe the physical sample used in the experiments presented later.

1.1 The electron-nuclear system

The system of interest here is that of an electron spin coupled to nuclear spins. It has been shown that universal control in a hyperfine coupled electron-nuclear system is achievable with only control on the electron spin provided that the hyperfine interaction is not diagonal in the electron Zeeman basis [36].

We focus mainly on systems of one electron coupled to one spin-1/2 nucleus. The Hamiltonian is the sum of the Zeeman terms for the electron and the nucleus and the hyperfine coupling between the two spins,

$$H = H_Z^e + H_Z^n + H_{HF} \tag{1.1}$$

The Zeeman Hamiltonian describes the interaction of the magnetic moment of the spin with the external field,

$$H_Z = -\vec{\mu} \cdot \vec{B}_0 \tag{1.2}$$

As in classical electromagnetism, it is energetically favorable for the magnetic dipole to be aligned or anti-aligned with the external field, $\vec{B}_0$. In terms of the spin operators, the Zeeman Hamiltonians are,

$$\begin{aligned} H_Z^e &= \beta_B \vec{B}_0 \hat{\mathbf{g}}_e \vec{S} \\ H_Z^n &= \beta_N \vec{B}_0 \hat{\mathbf{g}}_n \vec{I} \end{aligned} \tag{1.3}$$

where β_B is the Bohr magneton, and β_N the nuclear magneton. The g-tensors, $\hat{\mathbf{g}}_e$ and $\hat{\mathbf{g}}_n$, contain any anisotropy of the spin interaction with $\vec{B}_0$ such as the spin-orbit coupling for electrons or the chemical shift for nuclei. Here we neglect any off-diagonal components of the g-tenors, and we can write the Zeeman terms as

$$H_Z^e = \hbar\gamma_e \vec{B}_0 \cdot \vec{S} = \hbar\omega_S S_z$$
$$H_Z^n = \hbar\gamma_n \vec{B}_0 \cdot \vec{I} = \hbar\omega_I \vec{I}_z \tag{1.4}$$

where the gyromagnetic ratio is defined $\gamma_e = g_e\beta_B/\hbar$ and the Larmor frequency $\omega_s = \gamma_e B_0$. The gyromagnetic ratio of an isolated electron is 28GHz/T, and γ_n for a proton is 42MHz/T. From these numbers we see that the electron Zeeman interaction is dominant with a strength $\gamma_e/\gamma_n = 660$ times that of the proton Zeeman energy. This ratio is even greater for larger nuclei. The electron and nuclear spins are coupled through the hyperfine interaction,

$$H_{HF} = \vec{S}\hat{\mathbf{A}}\vec{I} \tag{1.5}$$

A is the tensor operator for the hyperfine coupling. The Hyperfine coupling is the sum of two contributions: the Fermi contact and dipole-dipole interactions.

$$H_{HF} = H_{FC} + H_{DD} \tag{1.6}$$
$$H_{FC} = \frac{2}{3}\mu_0\gamma_S\gamma_I \left|\Psi_0(0)\right|^2 \vec{S}\cdot\vec{I} \tag{1.7}$$
$$H_{DD} = \frac{\mu_0}{4\pi}\gamma_S\gamma_I \left(\frac{3\left(\vec{S}\cdot\vec{r}\right)\left(\vec{r}\cdot\vec{I}\right)}{r^5} - \frac{\vec{S}\cdot\vec{I}}{r^3}\right) \tag{1.8}$$

The Fermi contact interaction arises from the overlap of the electron wavefunction, $\Psi_0(\vec{r})$, at the nucleus ($\vec{r} = 0$). The dipole-dipole interaction is the potential between two magnetic dipoles, which depends on the orientation of the spins relative to the external field and falls off as the cube of the distance between the spins [77, 53, 28]. The Fermi contact term is isotropic, while the dipole-dipole Hamiltonian contains both isotropic and anisotropic components. The hyperfine interaction is independent of the external field and can have a magnitude up to the order of 100MHz depending on the system.

The dipole-dipole interaction is often expanded into the dipolar alphabet [82]:

$$H_{DD} = \frac{\mu_0}{4\pi}\frac{\gamma_S \gamma_I}{r^3}\left[A + B + C + D + E + F\right] \tag{1.9}$$

$$\begin{aligned}
\text{with} \qquad A &= I_z S_z \left(1 - 3\cos^2\theta\right) \\
B &= -\frac{1}{4}\left(I_+ S_- + I_- S_+\right)\left(1 - 3\cos^2\theta\right) \\
C &= -\frac{3}{2}\left(I_+ S_z + I_z S_+\right)\sin\theta\cos\theta e^{-i\phi} \\
D &= -\frac{3}{2}\left(I_- S_z + I_z S_-\right)\sin\theta\cos\theta e^{-i\phi} \\
E &= -\frac{3}{4} I_+ S_+ \sin^2\theta e^{-2i\phi} \\
F &= -\frac{3}{4} I_- S_- \sin^2\theta e^{-2i\phi}
\end{aligned}$$

Here, r is the distance between the two spins, and θ and ϕ are the angles that the vector $\hat{r}$ makes with the external field. A and B are the zero quantum terms, with B driving spin-spin flip-flop interaction. C and D, the single quantum terms, are interactions which flip one spin depending on the state of the other, and the double quantum terms E and F induce mutual flip-flips.

The electron spin operator, $\vec{S}$, is quantized along the direction of $\vec{B}_0$; because of the magnitude of the electron Zeeman energy, this defines the quantization axis for this system. In the absence of any other interaction, the nuclear spin would also be quantized along the external field. The hyperfine interaction, however, mixes the nuclear Zeeman states.

At high field, for example at 1T, the electron Zeeman interaction is 28 GHz, while the proton Zeeman interaction is 42 MHz and the hyperfine interaction is typically within the range of kiloHertz to hundreds of megaHertz (although it can be up to a gigaHertz for certain semiconductor systems). Clearly the electron Zeeman term dominates, while the nuclear Zeeman and hyperfine interactions are perturbations. The electron spin is therefore a good quantum number, and the nuclear spin is not. The state of the electron spin does not depend on the state of the nuclear spin, but a flip of the electron spin will affect the nuclear spin state through the hyperfine coupling. Thus we can make the secular approximation, where we keep only terms which commute with $\hat{S}_z$. Considering just the isotropic hyperfine interaction, the term that commutes with $\hat{S}_z$ is

$$H_{iso} = A_{zz} I_z S_z \tag{1.10}$$

The dipole-dipole Hamiltonian contains additional terms that remain in the secular approximation, such as $I_x S_z$ and IyS_z.

$$H_{aniso} = A_{zx} I_x S_z + A_{zy} I_y S_z \tag{1.11}$$

where the A_{zi} are the elements of the hyperfine tensor written in the basis of the principal axis system. We can simplify the anisotropic interaction to a single term by performing a frame transformation on the hyperfine Hamiltonian using the rotation operator,

$$U = e^{i\phi I_z}. \tag{1.12}$$

The hyperfine interaction in this frame is

$$U^{\dagger} H_{HF} U = e^{-i\phi I_z} \left[A_{zz} I_z S_z + A_{zx} I_x S_z + A_{zy} I_y S_z \right] e^{i\phi I_z} \tag{1.13}$$

$$= A_{zz} I_z S_z + A_{zx} \left[\cos\phi I_x S_z - \sin\phi I_y S_z \right] + A_{zy} \left[\cos\phi I_y S_z + \sin\phi I_x S_z \right] \tag{1.14}$$

When $\phi = \arctan\left(\frac{A_{zy}}{A_{zx}}\right)$ the hyperfine Hamiltonian is

$$H_{HF} = A I_z S_z + B I_x S_z \tag{1.15}$$

where $A = A_{zz}$ and $B = \sqrt{A_{zx}^2 + A_{zy}^2}$.

The complete Hamiltonian for one electron and one nucleus under the secular approximation is

$$H = \omega_S S_z + \omega_I I_z + A I_z S_z + B I_x S_z \tag{1.16}$$

with $\omega_S = \gamma_e B_0$ and $\omega_I = \gamma_n B_0$.

1.2 N-N interactions and Spin Diffusion

As will be discussed later, in a typical DNP experiment the nuclear spins coupled directly to electron spins are polarized, and the polarization is then transferred to the nuclear spins far from the electron through nuclear-nuclear interactions. Our model system must include a nuclear spin bath which is connected via dipole-dipole interactions. The dipole-dipole interaction between like nuclear spins has the same form as Eq. (1.9). This interaction is typically on the order of tens of kiloHertz. The nuclear Zeeman energy is megaHertz, so when we take the secular approximation in the system of many nuclei, we retain the terms which do not perturb the energy levels. Only A and B in the dipolar alphabet are energy conserving when the spins are the same. Thus the dipole-dipole Hamiltonian for a system of many nuclei is

$$H_D^N = \hbar \sum_{i<j} b_{ij} \left(2I_z^i I_z^j - \frac{1}{2} \left(I_+^i I_-^j + I_-^i I_+^j \right) \right) \tag{1.17}$$

$$b_{ij} = \frac{\gamma^2 \hbar}{2} \frac{1 - 3\cos^2\theta_{ij}}{r_{ij}^3} \tag{1.18}$$

This Hamiltonian drives the process known as spin diffusion. Consider the simplified case when dipole-dipole interaction occur only between nearest neighbors. The rate, W, of the flip-flop transition is proportional to the matrix element $\langle \uparrow\downarrow | H_D^N | \downarrow\uparrow \rangle$. In a chain of spins each separated by a distance a, under a classical model of diffusion, the change of polarization for a single spin at position x_0 is described by the following rate equation [2, 8],

$$-\frac{dp(x_0)}{dt} = W\left[p(x_0 + a) + p(x_0 - a) - 2p(x_0)\right] = Wa^2 \frac{d^2 p}{dx^2} \tag{1.19}$$

From the second equality we see that this is a diffusion equation with diffusion coefficient Wa^2. In full generality, considering three dimensions and interactions between all pairs of spins, the diffusion equation is

$$-\frac{dp}{dt} = D\nabla^2 p + \sum_i \frac{C}{r_i^6}(p - p_0) \tag{1.20}$$

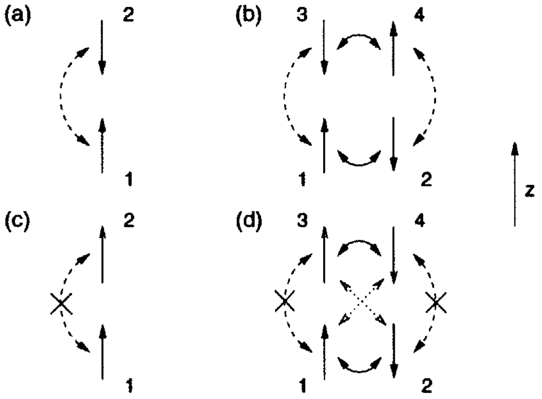

Figure 1-1: Figure from [12]. (*a*) Zeeman order diffuses when neighboring spins can exchange states. (*b*) Dipolar order states can diffuse in two directions. (*c*) Zeeman order cannot propagate when neighboring spins are in the same state, but (*d*) dipolar order still has another direction available for diffusion.

where D is the diffusion coefficient and C/r_i^6 describes the relaxation rate for each nuclear spins, i, at a distance r_i from the electron. Determining D theoretically is a difficult multibody problem. Studies on this subject have used Redfield's method of moments and linear response theory to calculate diffusion coefficients and correlation functions in dipolar coupled spin systems[32, 33].

Note also that in the dipolar coupled nuclear spin system, the spin magnetization is not the only conserved quantity. The dipolar energy is also conserved, and diffusion of the dipolar order also occurs under the Hamiltonian in Eq. (1.17). The diffusion rate of the dipolar ordered two-spin state can actually be faster than that of the Zeeman ordered single spin state. This can be seen simply by considering the paths of diffusion for each quantity (see Fig. (1-1). Zeeman order diffusion requires mutual spin flip-flops; if two neighboring spins are in the same state there cannot be any evolution. The four spin interaction required for dipolar order to diffuse can occur through flip flops in a perpendicular direction if two neighboring spins are aligned [12]. There is an additional degree of freedom for dipolar order to diffuse.

Spin diffusion is essential in DNP experiments. In a sample where the electron spins are dilute, there will be some nuclei directly coupled to the electron spin and many more nuclei far from the electron with small hyperfine couplings. As the dipolar

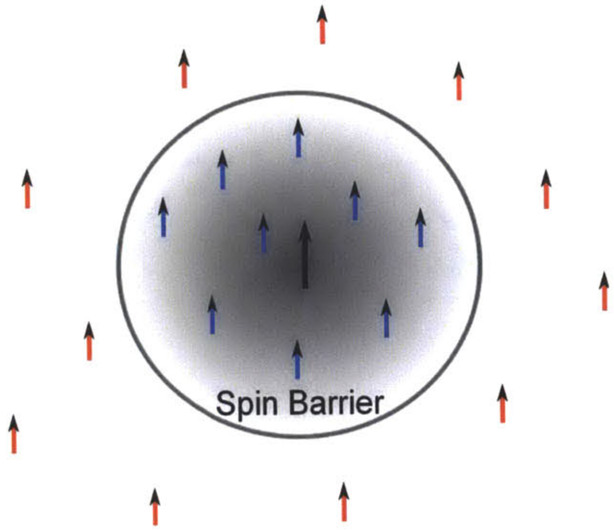

Figure 1-2: Spin diffusion across a spin barrier with nuclei inside the barrier coupled to a central electron and dipolar coupled to nuclei in the bulk.

coupling falls of as r^{-3} these couplings become small quickly with the distance from the nuclear spin. These distant nuclei can still be polarized, however, through spin diffusion.

The nuclear spins close to the electron defect will have an energy mismatch with the bulk nuclei though due to the large hyperfine coupling. This gives rise to what is known as the spin-diffusion barrier, a region of polarized nuclei close to the electron spin which cannot transfer their polarization outside the region to the weakly coupled nuclei [75]. When observing the bulk nuclei, spin diffusion will likely be the rate determining step in the polarization build up time.

1.3 Experimental System

The system chosen for this experiment is irradiated malonic acid (see Fig. 1-3). After X-ray irradiation the central carbon has one unpaired electron which is hyperfine coupled to the neighboring hydrogen nucleus. Malonic acid is a well characterized sample widely used in ESR [26, 80]. Malonic acid has a triclinic crystal structure with two molecules per unit cell. The nearest methyl-group protons have a dipolar coupling on the order of 60 kHz [31].

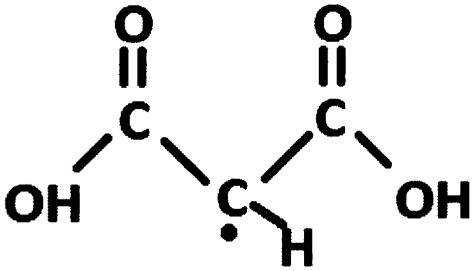

Figure 1-3: Malonic acid with one unpaired electron.

The Hamiltonian for this system under the secular approximation is

$$H = \omega_S S_z - \omega_I I_z + A I_z S_z + B I_x S_z \tag{1.21}$$

In an external field of 3406 G, the electron Larmor frequency, ω_S, is 9.59 GHz, the nuclear resonance, ω_I is 14.57 MHz. The terms A and B depend on the orientation of the crystal in the field. The anisotropic hyperfine term is maximized when the $\hat{a}$-$\hat{c}$ plane of the crystal is at 45° to the external $B_o\hat{z}$ field. In this orientation the isotropic and anisotropic parts of the hyperfine coupling are -42.7 MHz and 14.2 MHz respectively.

The malonic acid sample used in the experiments here was a single crystal irradiated for 5 hours with 8 keV X-rays and subsequently annealed at 45°C for 15 hours. We mapped the orientation hyperfine coupling by rotating the sample in a CW-ESR spectrometer (Fig. 1-4) and measuring the splitting of the two hyperfine peaks as a function of the rotation angle (Fig. 1-5). The anisotropic hyperfine term is maximized when the sample is oriented so that the splitting in the CW spectrum is 15 G. From the amplitude of the CW spectrum we estimate that the defects in the sample are separated by approximately 100 nm. T_1 of the electron for this sample was measured to be 16 μs.

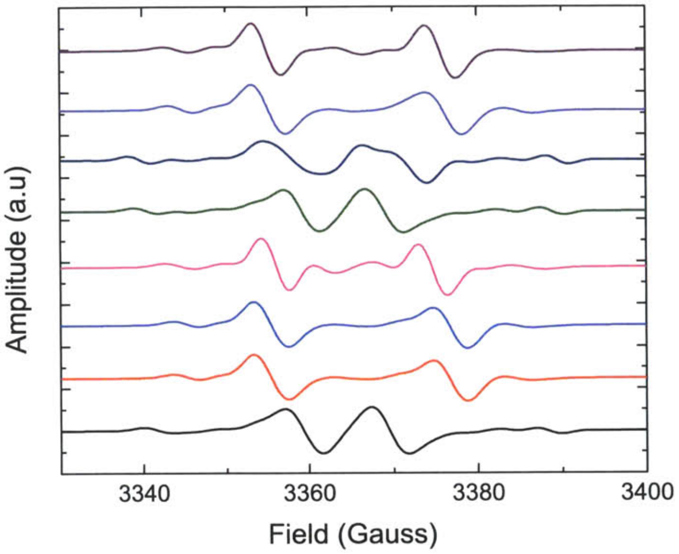

Figure 1-4: Continuous wave spectra of irradiated malonic acid at different orientations with respect to the external field. The two main dispersive peaks indicate electrons which are hyperfine coupled to nuclear spins in either the up or down states. The value of the splitting indicates the strength of the hyperfine coupling, which varies with the orientation of the crystal. The spectra are plotted successively for sample orientations rotated 15° from the previous plot. The magnitude of this signal indicates the sample has on the order of 10^{15} electron spins.

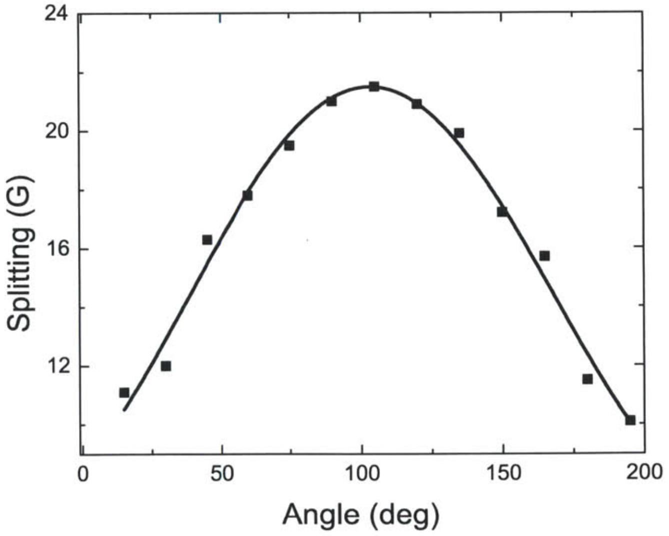

Figure 1-5: Hyperfine splitting as a function of the rotation angle.

Chapter 2

Open Quantum Systems and Superoperator Representations

We now discuss the evolution of the electron-nuclear hyperfine coupled system. We are interested in dynamics including the effects of the environment. We will need to account for relaxation processes in order to find control sequences and to simulate DNP in our model system. One can derive evolution in an open quantum system using several different superoperator representations, which we describe in this chapter.

Closed system dynamics are driven by a unitary operator which is determined by the system Hamiltonian. To include the interactions with environment, we must find Liouville space operators which act on the density matrix, ρ, that contains all information about the state of the system. Unlike closed quantum systems, open quantum dynamics are non-unitary and must be described by a completely positive, trace-preserving (CPTP) map, Λ, which takes $\rho(t=0)$ to $\rho(t)$,

$$\rho(t) = \Lambda_t(\rho(t_0)) \tag{2.1}$$

We will also refer to Λ as a superoperator, which is typically defined as a linear operator acting on a space of linear operators. The CPTP property of Λ is necessary to preserve the linearity and normalization of ρ [50, 4].

Consider the Hilbert space $\mathcal{H}_S \otimes \mathcal{H}_E$, the space of the combined system and environment - in the context of NMR this would be the system of a spin which decoheres due to fluctuating fields in the local environment. The evolution of the combined system is unitary

$$\rho_{SE}(t) = U(t)\rho_{SE}(0)U^{\dagger}(t) \tag{2.2}$$

If we want to find the evolution of only the system, we must trace out the environment. Assuming the initial state has no correlations with the environment, the density matrix can be written:

$$\begin{aligned} \rho_S(t) &= \Lambda(\rho_S(0)) = Tr_E\left[U(t)\rho_S(0) \otimes |\psi\rangle_E \langle\psi|_E U^{\dagger}(t)\right] \\ &\equiv \sum_k A_k \rho_S(0) A_k^{\dagger} \end{aligned} \tag{2.3}$$

Here, the operator $A_k = \langle k| U(t) |\psi\rangle$ acts only on the system Hilbert space.

As we are interested in magnetic resonance systems, we mention that the density matrix, ρ, mathematically defines the total state of the spin system with the diagonal terms indicating the state populations and the off-diagonal terms representing the coherences between states. Decay of the diagonal terms corresponds physically to T_1 relaxation, which returns the populations to their thermal equilibrium values. In the general open quantum system formalism, this type of relaxation is described by an amplitude damping channel. Similarly, loss of coherence affects the off-diagonal terms. Physically this looks like dephasing, or T_2 relaxation, and is achieved operationally through a phase damping channel.

2.0.1 Kraus Operators

There are several superoperator representations we can use to describe open quantum dynamics in an NMR setting. One choice is the Kraus operator or operator sum representation [65, 47]. The set A_k in Eq.(2.3) are called Kraus operators, and the map Λ as defined in Eq. 2.3 is a valid superoperator as long as the constraint,

$$\sum_k A_k^\dagger A_k = \mathbb{I} \tag{2.4}$$

is satisfied. This requirement ensures the trace preserving property of the quantum dynamical semigroup.

Kraus operators are not a unique representation of a given map of open quantum dynamics, but, according to the Kraus Representation theorem, if a superoperator can be written as a Kraus decomposition then it is a completely positive map [46].

Amplitude Damping

For a single spin-1/2 the amplitude damping channel is given by two Kraus operators [65, 71],

$$A_0 = \begin{pmatrix} 1 & 0 \\ 0 & \sqrt{1-\gamma} \end{pmatrix}, A_1 = \begin{pmatrix} 0 & \sqrt{\gamma} \\ 0 & 0 \end{pmatrix} \tag{2.5}$$

If the initial state of this two level system is

$$\rho = \begin{pmatrix} \rho_{00} & \rho_{01} \\ \rho_{10} & \rho_{11} \end{pmatrix} \tag{2.6}$$

and the map $\Lambda(\rho)$ defined by the operators in Eq. (2.5) is applied repeatedly, then after n iterations the state is

$$\rho' = \begin{pmatrix} 1-(1-\gamma)^n\rho_{11} & (\sqrt{1-\gamma})^n\rho_{01} \\ (\sqrt{1-\gamma})^n\rho_{10} & (1-\gamma)^n\rho_{11} \end{pmatrix} \tag{2.7}$$

$$\tag{2.8}$$

We set $\gamma = \Gamma_1 t_n$ to connect these abstract operators to a physical system. Γ_1 is the rate of longitudinal relaxation and is equal to the inverse of T_1. Then as $n \to \infty$ we have

$$\rho' \Rightarrow \begin{pmatrix} 1-e^{-\Gamma_1 t}\rho_{11} & e^{-\Gamma_1 t/2}\rho_{01} \\ e^{-\Gamma_1 t/2}\rho_{10} & e^{-\Gamma_1 t}\rho_{11} \end{pmatrix} \tag{2.9}$$

This map drives ρ to a pure state in which the spin is fully polarized in the ground state. The diagonal terms decay simultaneously, as is expected for T_1 relaxation. A similar set of Kraus operators that drive the system towards a mixed state or the thermal equilibrium state is

$$\begin{aligned} A_1 &= \sqrt{p}\begin{pmatrix} 1 & 0 \\ 0 & \sqrt{\epsilon} \end{pmatrix} & A_2 &= \sqrt{p}\begin{pmatrix} 0 & \sqrt{1-\epsilon} \\ 0 & 0 \end{pmatrix} \\ A_3 &= \sqrt{1-p}\begin{pmatrix} \sqrt{\epsilon} & 0 \\ 0 & 1 \end{pmatrix} & A_4 &= \sqrt{1-p}\begin{pmatrix} 0 & 0 \\ \sqrt{1-\epsilon} & 0 \end{pmatrix} \end{aligned} \tag{2.10}$$

Where $\epsilon = \exp(-t/T_1)$ and $p = \exp(-\hbar\omega/k_bT)$. The thermal equilibrium polarization is defined by the temperature, T, and the Larmor frequency of the spin in the external field, ω.

Phase Damping

As we did for amplitude damping, we can also write out Kraus operators for the phase damping channel and connect them to T_2 relaxation. The Kraus operators for phase damping are

$$A_0 = \begin{pmatrix} 1 & 0 \\ 0 & \sqrt{1-\lambda} \end{pmatrix}, \ A_1 = \begin{pmatrix} 0 & 0 \\ 0 & \sqrt{\lambda} \end{pmatrix} \tag{2.11}$$

If we set $\lambda = \Gamma_2 t_n$ with $\Gamma_2 = 1/T_2$ and apply the Kraus operators repeatedly, this map takes ρ to

$$\rho' = \begin{pmatrix} 1-\rho_{11} & e^{-\Gamma_2 t}\rho_{01} \\ e^{-\Gamma_2 t}\rho_{10} & \rho_{11} \end{pmatrix} \tag{2.12}$$

where $\Gamma_2 = 1/T_2$ is the transverse relaxation rate. These operators reduce the amplitude of the off diagonal terms, indicating a loss of coherence.

Choi Matrix

As the Kraus operators are not unique, in order to increase the speed of simulations it is helpful to find the smallest set of Kraus operators possible. Simulations of systems with several processes occurring simultaneously in a system require multiple sets of Kraus operators, and one often wishes to simplify the numerics by finding the minimum number of operators needed to describe these complex dynamics.

One procedure for constructing this set begins with the Choi matrix, which is defined as

$$\Lambda_C = (\mathbb{I} \otimes \Lambda) \sum_{ij} E_{ij} \otimes E_{ij} = \sum_{ij} E_{ij} \otimes \Lambda(E_{ij}) \tag{2.13}$$

where $E_{ij} = |i\rangle \langle j|$ and the vectors $\{|i\rangle, |j\rangle\}$ form a basis of the Hilbert space. We can derive the Kraus operators from the columns of the Choi matrix [49, 34, 19].

From Eq.(2.13) the next step is to rewrite Λ_c in terms of its normalized eigenvectors, $|a_k\rangle$,

$$\Lambda_C = \sum_k |a_k\rangle \langle a_k| \tag{2.14}$$

The columns of Λ_C now form a set of columnized Kraus operators $\{A_k\}$ satisfying Eqs. (2.3) and (2.4) with d^2 operators in the set, where d is the dimension of the Hilbert space.

2.0.2 Lindblad Form

Another useful form of the superoperator is the Lindbladian. If we consider the case when the state of the system does not depend on its history, i.e. Markovian dynamics, we can evolve the system by applying a generator, $\mathcal{L}$[50, 34], similar to the Hamiltonian in closed system dynamics,

$$\frac{d\rho(t)}{dt} = \mathcal{L}\rho(t) \tag{2.15}$$

We can separate $\mathcal{L}$ into a unitary operator and a dissipator,

$$\mathcal{L}\rho = -i\left[H, \rho\right] + \mathcal{D}(\rho) \tag{2.16}$$

The dissipator, $\mathcal{D}$, leads to decoherence dynamics such as dephasing or return to thermal equilibrium. $\mathcal{D}$ is given by

$$\mathcal{D} = \frac{1}{2}\sum_{k=0}^{d^2-1}\left(\left[L_k, \rho L_k^\dagger\right] + \left[L_k\rho, L_k^\dagger\right]\right) \tag{2.17}$$

The L_k are the Lindblad jump operators. These operators can be derived from the Kraus operators. Consider, for example, the amplitude damping channel defined by the Kraus operators in Eq.(2.5). In order to find the corresponding Lindblad form, we must take the Kraus operators in the continuous time limit: as the time step $\Delta t \to 0$, we can make the approximation,

$$\sqrt{1-\gamma} = 1 - \frac{\gamma}{2} + O(\Delta t^2) \tag{2.18}$$

and using the raising and lowering operators $\sigma_\pm = (\sigma_x \pm i\sigma_y)/2$ rewrite the Kraus operators,

$$\begin{aligned} A_0 &\approx \mathbb{I} - \frac{\gamma}{2}\sigma_-\sigma_+ \\ A_1 &= \sqrt{\gamma}\sigma_+ \end{aligned} \tag{2.19}$$

In the continuous time limit $\mathcal{L}$ satisfies

$$\mathcal{L}\rho(t) = \frac{d\rho(t)}{dt} = \lim_{\Delta t\to 0}\frac{\rho(t+\Delta t) - \rho(t)}{\Delta t} \tag{2.20}$$

After applying the Kraus operators to find $\rho(t + \Delta t)$,

$$\begin{aligned}\mathcal{L}\rho(t) &= \lim_{\Delta t \to 0} \frac{A_0\rho(t)A_0^\dagger + A_1\rho(t)A_1^\dagger - \rho(t)}{\Delta t} \\ &= \lim_{\Delta t \to 0} \frac{-\frac{\gamma}{2}\sigma_-\sigma_+\rho(t) - \frac{\gamma}{2}\rho(t)\sigma_-\sigma_+ + -\frac{\gamma^2}{4}\sigma_-\sigma_+\rho(t)\sigma_-\sigma_+ + \gamma\sigma_+\rho(t)\sigma_-}{\Delta t}\end{aligned} \tag{2.21}$$

Making the substitution $\gamma = \Gamma_1 t/2$ and taking the limit gives,

$$\mathcal{L}\rho(t) = -\frac{\Gamma_1}{2}\sigma_-\sigma_+\rho - \frac{\Gamma_1}{2}\rho\sigma_-\sigma_+ + \Gamma_1\sigma_+\rho\sigma_- \tag{2.22}$$

Thus the Lindblad form for amplitude damping has one Lindblad operator, $L_1 = \sqrt{\Gamma_1}\sigma_+$.

An essential difference between the Kraus sum and Lindblad forms is that the Lindblad is only valid for describing Markovian dynamics. The advantage of the Lindblad superoperator, however, is that the operators are continuous while the Kraus operators are applied in discrete time steps. When the Kraus operators do not commute with the drift Hamiltonian they must be calculated for short enough times t relative to all interactions such that the discrete evolution is an accurate representation of the system dynamics.

2.0.3 Matrix Form of the Superoperator

It is often useful in simulations to columnize the density matrix and apply the superoperator as an $d^2 \times d^2$ matrix in Liouville space, where d is the dimension of the corresponding Hilbert space. This form is useful as it requires only the multiplication of a vector by a matrix. In this representation the equation of motion is

$$\mathrm{col}(\rho(t)) = \mathcal{S}(t)\mathrm{col}(\rho) \tag{2.23}$$

If another form of the superoperator is known, one can find the matrix form. From the Kraus operators $\{A_k\}$, the matrix $\mathcal{S}$ is [34]

$$\mathcal{S}(t) \equiv \sum_k A_k(t)^* \otimes A_k(t) \tag{2.24}$$

It is possible to convert between all of the superoperator representations. While all forms should produce the same evolution, the choice of superoperator will depend on the difficulty of the numerics, knowledge of the system, and time scales of the problem.

Chapter 3

Dynamic Nuclear Polarization

This chapter describes the mechanisms of dynamic nuclear polarization (DNP) in an electron-nuclear system. Several pathways that lead to a polarized nuclear state can be allowed in a DNP experiment, and we will discuss in the following chapters how to excite only one and suppress others.

DNP has a long history in NMR as a tool for increasing the polarization of the nuclear spin. Recently research in DNP has focused on high field experiments [55], biomolecular DNP [73, 89], solid state DNP with magic-angle spinning [90, 24], and dissolution DNP [52, 21]. Increase in nuclear polarization can be beneficial for many NMR experiments, especially when sensitivity is an issue.

The potential uses of DNP in quantum information include the transfer and storage of information. DNP also provides a means of purifying states that are mixed at thermal equilibrium.. In solid state electron-nuclear systems DNP can be used to initialize ensembles of nuclei, effectively removing entropy from the nuclear ensemble.

3.1 Hyperpolarization of Nuclear Spins

Consider a spin ensemble at thermal equilibrium in an external magnetic field. Among the spins in the ensemble, slightly more will occupy the lower energy state. This difference between populations of the ground and excited states is given by the Boltzmann distribution. For a spin 1/2,

$$\frac{N_-}{N_+} = e^{-\frac{\Delta E}{k_B T}} = e^{-\frac{\hbar\gamma B}{k_B T}} \tag{3.1}$$

with k_B the Boltzmann constant, T the temperature, B the applied field, and γ the gyromagnetic ratio of the spin. The polarization is given by

$$P = \frac{N_- - N_+}{N_- + N_+} = \frac{e^{-\frac{\hbar\gamma B}{k_B T}} - 1}{e^{-\frac{\hbar\gamma B}{k_B T}} + 1} \approx -\frac{\hbar\gamma B}{2k_B T} \tag{3.2}$$

NMR signals are proportional to the nuclear polarization. Thus increasing polarization will increase the strength of the NMR signal. Spins can be polarized via the 'brute force' method, i.e. increasing the field or decreasing the temperature. Proton spins in 2.35 T field at room temperature have a polarization of 8×10^{-6}, which can be brought up to 2.3×10^{-3} in 9.4 T and at liquid helium temperature. There are, however, experimental limits to how high B_0, and how low T, can be made. Additionally many properties of a sample vary with changing field or temperature. At high fields mixing of hyperfine coupled nuclear states will be smaller, for example, because the Zeeman energy increases with field while the hyperfine coupling is constant. At low temperature relaxation times may become long and cause experiments to be impractically long.

There are several methods of hyperpolarizing nuclear spins. Chemically-induced dynamic nuclear polarization (CIDNP) is used to enhance NMR signals of proteins and to characterize reaction mechanisms. CIDNP relies on a nuclear spin selective recombination of radical pairs through an intersystem crossing. This method is restricted to those chemicals that can create radical pairs that lead to a polarized nuclear state [60].

Para-hydrogen induced DNP is similarly limited to only those samples which can be polarized through certain chemical reactions, in this case with para-hydrogen as a polarizing agent. At low temperatures the singlet state of two hydrogen nuclei (para-H_2) is energetically favorable over the triplet state (ortho-H_2), such that over

99% of H_2 is in the singlet state at 20K. The polarization can be transferred from the hydrogen state to molecules to be studied [61].

Optical pumping has also been used with success to polarize noble gases, He-3 and Xe-129 in particular [86, 35]. Magnetic resonance imaging of lungs with polarized noble gases is now a well established technique that provides dynamic information on lung function that is unavailable through other imaging techniques [91].

All of these methods are restricted in their application to whatever chemical species will react with the polarizing agent or, in the case of optical pumping, to noble gases. Dynamic nuclear polarization using microwave irradiation is more broadly applicable to any sample that has unpaired electrons spins hyperfine-coupled to nuclear spins. Such samples can be organic radicals or doped semiconductors, and DNP can be used in liquid or solid state NMR at a wide range of fields.

The study of DNP began when Overhauser first proposed a method of polarizing nuclei in metals using microwave irradiation in 1953 [66]. He showed that the polarization of the electrons could be transferred to the nuclei, resulting in a nuclear polarization enhancement equal to the ratio γ_e/γ_n (= 660 for hydrogen nuclei). Carver and Slichter demonstrated this polarization enhancement experimentally in 1956 in liquid samples of metallic ions [16]. The original DNP experiments polarized the nuclear spins through what is now known as the Overhauser Effect (OE) and was thought to be only possible in metallic and liquid samples. Abragam later described a method of polarization enhancement in solids, now called the solid effect (SE)[3].

All methods of DNP require that the nuclear Zeeman states not be eigenstates of the system. Otherwise the necessary transitions for transferring polarization are forbidden. Mixing of the nuclear Zeeman states occurs via the anisotropic hyperfine Hamiltonian discussed in Chapter 1. In particular, there must be a strong electron-nuclear dipolar interaction,

$$H_{DD} = \frac{\mu_0}{4\pi}\gamma_S\gamma_I\left(\frac{3\left(\vec{S}\cdot\vec{r}\right)\left(\vec{r}\cdot\vec{I}\right)}{r^5} - \frac{\vec{S}\cdot\vec{I}}{r^3}\right) \tag{3.3}$$

The Overhauser effect and solid effects are single electron processes, in which the electron spin state is disturbed from equilibrium. The Overhauser effect is dominant in liquid state DNP and at low fields where there is strong mixing of the nuclear Zeeman states. The solid effect is stronger in solid state systems at low temperatures. In systems with large electron concentrations, additional DNP mechanisms are possible, such as the cross effect and thermal mixing. In the following sections we will look at the mechanisms that drive each of these processes.

3.2 Overhauser Effect

We consider first the case when the microwave irradiation saturates the two electron resonances. If the nuclear states are mixed the system will try to establish thermal equilibrium through electron-nuclear flip-flops (or flip-flips if there is a double quantum relaxation process), or, in other words, through cross relaxation between the electron and nuclear spins. The process is the Overhauser effect and is depicted in Fig 3-1.

As the electron spin is saturated, polarization builds up on the nuclear spin. The final nuclear polarization depends on several factors, such as the efficiency of the saturation and the relevant relaxation rates. The theoretical limit of the nuclear polarization enhancement can be determined using a set of rate equations.

3.2.1 Rate Equations

We can use a fully quantum approach (as will be seen later) or we can follow the original analysis using rate equations to analyze the polarization transfer and calculate the final nuclear enhancement [83]. In order to set up the rate equations, we need to consider all possible transitions in the four level system. The microwave saturation flips the electron spin, and the cross relaxation drives the flip-flop transition. For complete transfer of polarization from the electron to the nucleus there must also be a reset of the electron spin as it is being saturated; this resetting is achieved through T_1 relaxation of the electron. These transitions for a general two spin-1/2 system are shown in Fig. 3-2. Here W_2 is the rate of double quantum transitions driven by a

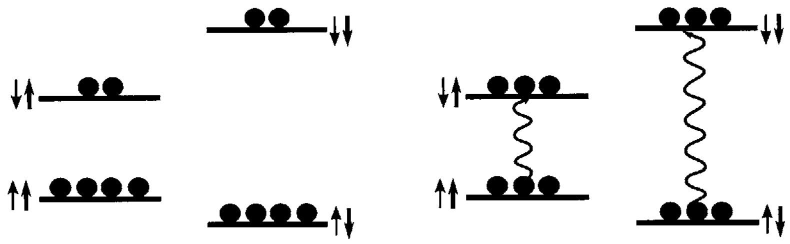

(a) Thermal Equilibrium (b) Saturate Electrons

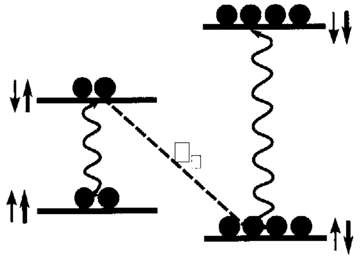

(c) Final Nuclear Polarization

Figure 3-1: Overhauser Effect

flip-flip type relaxation, which could also be present.

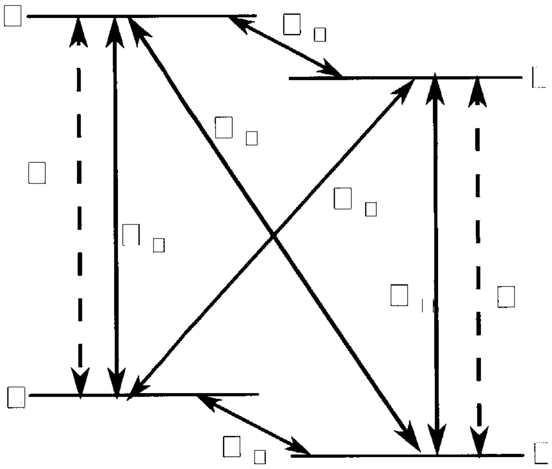

Figure 3-2: All transitions for the Overhauser effect.

For the system in Fig. 3-2 we can write a set of equations for the populations, N_i, for each energy level $|i\rangle$ including transitions between every pair of levels. We include the electron and nuclear T_1 relaxation through the rates W_e and W_n. The zero quantum and double quantum cross relaxation rates are W_0 and W_2. Lastly W is the rate of the transitions induced by the microwave field, in this case on resonance with the electron resonance.

$$
\begin{aligned}
\frac{d}{dt}N_1 =& -(W+W_e+W_2+W_n)(N_1-N_1^0)\\
&+W_n(N_2-N_2^0)+(W+W_e)(N_3-N_3^0)+W_2(N_4-N_4^0)\\
\frac{d}{dt}N_2 =& -(W+W_e+W_0+W_n)(N_2-N_2^0)\\
&+W_n(N_1-N_1^0)+W_0(N_3-N_3^0)+(W+W_e)(N_4-N_4^0)\\
\frac{d}{dt}N_3 =& -(W+W_e+W_0+W_n)(N_3-N_3^0)\\
&+(W+W_e)(N_1-N_1^0)+W_0(N_2-N_2^0)+W_n(N_4-N_4^0)\\
\frac{d}{dt}N_4 =& -(W+W_e+W_2+W_n)(N_4-N_4^0)\\
&+W_2(N_1-N_1^0)+(W+W_e)(N_2-N_2^0)+W_n(N_e-N_e^0) \qquad (3.4)
\end{aligned}
$$

where N_i^0 is the population of $|i\rangle$ at thermal equilibrium. W_n will be negligible compared to the other rates as the nuclear T_1 is a much longer process than the same for the electron. We can rewrite Eq. (3.4) in terms of the electron and nuclear polarizations,

$$
\begin{aligned}
P_e &= \frac{N_1+N_2-N_3-N_4}{\sum_i N_i}\\
P_n &= \frac{N_1-N_2+N_3-N_4}{\sum_i N_i} \qquad (3.5)
\end{aligned}
$$

and also define, for simplicity, the following,

$$
\begin{aligned}
\rho' &= W_2+W_0+2W_1\\
\rho &= W_2+W_0+2W_n\\
\sigma &= W_2-W_0
\end{aligned}
$$

After combining Eqs. 3.4 and 3.5, the rate equations reduce to:

$$
\frac{d}{dt}P_e = -\rho'(P_e-P_e^0)-\sigma(P_n-P_n^0)
$$

$$\frac{d}{dt}P_n = -\rho(P_n - P_n^0) - \sigma(P_e - P_e^0) \tag{3.6}$$

We now solve for P_n in the steady-state,

$$\begin{aligned}&\frac{d}{dt}P_n = 0\\ &\Rightarrow P_n = P_n^0 - \frac{\sigma}{\rho}(P_e - P_e^0)\end{aligned} \tag{3.7}$$

$$P_n = -\frac{P_n^0 + \sigma(P_e - P_e^0)}{\rho} \tag{3.8}$$

and find the nuclear polarization enhancement

$$\begin{aligned}\varepsilon &= \frac{P_n - P_n^0}{P_n^0}\\ &= \frac{\sigma}{\rho}\frac{P_e - P_e^0}{P_e^0}\frac{P_e^0}{P_n^0}\\ &= \xi S \frac{\gamma_e}{\gamma_n}\end{aligned} \tag{3.9}$$

where we have used the fact that the ratio of the initial polarizations is equal to γ_e/γ_n and defined the coupling factor, $\xi = \sigma/\rho$, and the saturation factor, $S = (P_e - P_e^0)/P_e^0$. The coupling factor quantifies the amount of polarization transferred through the zero quantum pathway versus the double quantum. The saturation factor is a measure of how well the microwave field equilibrates the electron Zeeman states. When the electron resonances are fully saturated, P_e goes to zero, and S is equal to one. The enhancement is largest when these factors are equal to one, and the nuclear polarization is enhanced by a factor of γ_e/γ_n. The coupling factor, ξ, is close to one when the nuclear relaxation time is small compared to the cross relaxation and when either one of the flip-flip or flip-flop process is much larger than the other. Typically $W_0 > W_2$, and σ is negative. When γ_e and γ_n have opposite sign, the nuclear enhancement is positive.

3.2.2 Transition Rates

Here we are interested in the rate of transitions between the zero quantum states due to a cross relaxation mechanism. The cross relaxation between the electron and nucleus is necessary for the Overhauser effect. The fast relaxing electron creates a local fluctuating field at the site of the nucleus, which induces a nuclear spin flip.

The transition rates for this process can be calculated according to relaxation theory [2]. The transition probabilities between pairs of states due to a Hamiltonian, $H'(t')$ are given by perturbation theory,

$$W_{jk} = \int_0^t \overline{\langle j| H'(t') |k\rangle \langle k| H'(t') |j\rangle} e^{-i\omega_{jk}(t'-t)} dt' + c.c. \tag{3.10}$$

The perturbing Hamiltonian that causes cross relaxation is the dipolar component of the hyperfine coupling. The largest contributions come from the C and D terms,

$$\begin{aligned} H'(t) &= \frac{\mu_0}{4\pi}\frac{\gamma_S\gamma_I}{r^3}\left[C+D\right] \qquad (3.11)\\ C &= -\frac{3}{2}\left(I_+S_z + I_zS_+\right)\sin\theta\cos\theta e^{-i\phi}\\ D &= -\frac{3}{2}\left(I_-S_z + I_zS_-\right)\sin\theta\cos\theta e^{-i\phi} \end{aligned} \tag{3.12}$$

Here the time dependence of $H'(t)$ comes from the time dependence of the spin operator $S_z(t)$ which varies as the electron spin relaxes [3]. In general, one can write the perturbation as a product of the spin operator and the fluctuating field [2], so for the C component of the dipolar interaction with the fluctuating field determined by $S_z(t)$ we have

$$H'(t) = S_z(t)\hat{C}'$$

with $C' = -\frac{3}{2}\frac{\mu_0}{4\pi}\gamma_S\gamma_I r^{-3}\sin\theta\cos\theta e^{-i\phi}I_+$. Eq. (3.10) reduces to

$$W_{jk} = \left|\langle j| \hat{C}' |k\rangle\right|^2 \int_{-\infty}^{\infty} \overline{S_z(t)S_z(t+\tau)} e^{-i\omega_I\tau} d\tau \tag{3.13}$$

where $\overline{S_z(t)S_z(t+\tau)}$ is the thermal average [3].

We can define the spectral density, $J(\omega)$,

$$J(\omega) = \int_{-\infty}^{\infty} \overline{S_z(t)S_z(t+\tau)} e^{i\omega_I \tau} d\tau \tag{3.14}$$

According to BPP relaxation theory, we assume that the correlation function, $\overline{S_z(t)S_z(t+\tau)}$, for T_1 relaxation of the electron can be represented by a single exponential [9]. Thus $J(\omega)$, the Fourier transform of $\overline{S_z(t)S_z(t+\tau)}$, is a Lorentzian, and the correlation time τ is T_1^e

$$J(\omega) = \frac{T_1^e}{1+\omega_I^2 T_1^{e2}}$$

Evaluating Eq. (3.13) using C' and $J(\omega)$ gives the result for the transition rate [3]:

$$W_x = T_x^{-1} = \frac{9}{2}\frac{\mu_0}{4\pi}\frac{\gamma_S\gamma_I}{r^6}(1+3\cos^2\theta)^2\frac{T_1^e}{1+\omega_I^2 T_1^{e2}} \tag{3.15}$$

An alternative approach for determining the cross relaxation rate is to consider the eigenstates of the system. The large anisotropic hyperfine interaction (due to C and D of the dipolar alphabet as mentioned previously) mixes the nuclear Zeeman states, so that the eigenstates include the hyperfine perturbation. Thus when the electron flips under T_1 relaxation, there is some probability that the transition will preserve the nuclear spin state and a non-zero probability that the T_1^e will populate a state with opposite nuclear spin alignment. This method is equivalent to the description of T_x discussed above and leads to the same expression for T_x [3]. We will continue to discuss the mixing of the nuclear Zeeman states in the next section in the context of another method of DNP.

3.3 Solid Effect

Here we consider a mechanism of DNP that directly polarizes the nuclear spin through excitations of transitions that require mutual flips of the electron and nuclear spins. This form of DNP is known as the solid effect. Irradiation of either one of the cross transitions (zero quantum or double quantum transition) as shown in Fig 3-3 will drive the system to a highly polarized nuclear spin state. These transitions are forbidden, however, unless there is an a term in the Hamiltonian that mixes the nuclear states, a condition that is satisfied when the anisotropic component of the hyperfine coupling is on the order of the nuclear Zeeman energy. Even at modest fields the electron Zeeman energy may be much larger than the hyperfine coupling and the nuclear Zeeman term. In this case we can take the secular approximation of the dipolar Hamiltonian discussed in Chapter 1 [3, 95]. The anisotropic components come from the C and D terms of the dipolar alphabet,

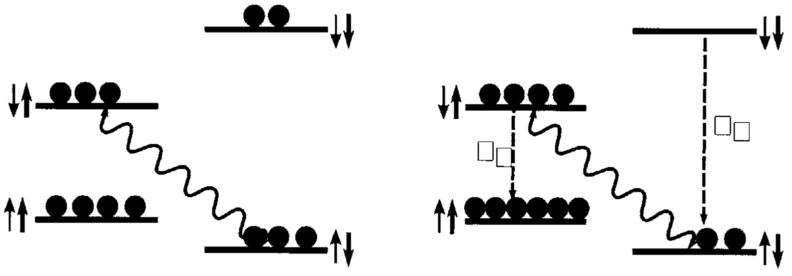

(a) Microwave Saturation (b) Final Nuclear Polarization

Figure 3-3: Solid Effect

$$H_{DD}^{aniso} = -\frac{\mu_0}{4\pi}\frac{3}{2}\frac{\gamma_e\gamma_n\hbar^2}{r^3}\sin\theta\cos\theta e^{-i\phi}\left(I^+S_z + I^-S_z\right) \tag{3.16}$$

The eigenstates of the electron-nuclear system with this perturbation to the Zeeman states are

$$\begin{aligned}
|\downarrow\alpha\rangle &= p\,|\downarrow\uparrow\rangle + q^*\,|\downarrow\downarrow\rangle \\
|\downarrow\alpha'\rangle &= p\,|\downarrow\uparrow\rangle - q\,|\downarrow\downarrow\rangle \\
|\uparrow\beta\rangle &= p\,|\uparrow\uparrow\rangle - q^*\,|\uparrow\downarrow\rangle \\
|\uparrow\beta'\rangle &= p\,|\uparrow\uparrow\rangle + q\,|\uparrow\downarrow\rangle
\end{aligned} \tag{3.17}$$

with

$$
\begin{aligned}
q &= \frac{3}{2}\frac{\gamma_e\gamma_n\hbar^2}{r^3}\frac{1}{\omega_n}\sin\theta\cos\theta e^{-i\phi} \\
p &= (1-qq^*)^{1/2} \approx 1
\end{aligned}
\tag{3.18}
$$

This mixing allows excitation of the forbidden transitions by the microwave field, $H' = \gamma_e B_1 S_x$ in the rotating frame. From Fermi's golden rule we find that the probability of the ZQ or DQ transitions during microwave excitation is determined by the mixing factor, q,

$$
\begin{aligned}
W_0 &\propto \langle\uparrow\alpha|\, H' \,|\downarrow\beta'\rangle \\
&= 4|q|^2\gamma_e B_1
\end{aligned}
\tag{3.19}
$$

Irradiation of the ZQ or DQ transitions will produce polarization of opposite signs. If the two transitions are unresolved, both can be excited simultaneously and partially cancel the effect.

3.3.1 Rate Equations

We can analyze the equations of motion for the solid effect as we did for the Overhauser effect. Assume that the ESR line is narrow and that microwaves are applied at the frequency corresponding to the ZQ transition (Fig.3-4). Assume we excite only the zero quantum transition with the microwave field, so W now is on resonance with the flip-flop resonance. Then the populations as a function of time are

$$
\begin{aligned}
\frac{d}{dt}N_1 =& -(W_e + W_2 + W_n)(N_1 - N_1^0) \\
& + W_n(N_2 - N_2^0) + W_e(N_3 - N_3^0) + W_2(N_4 - N_4^0) \\
\frac{d}{dt}N_2 =& -(W + W_e + W_0 + W_n)(N_2 - N_2^0) \\
& + W_n(N_1 - N_1^0) + (W_0 + W)(N_3 - N_3^0) + (W_e)(N_4 - N_4^0)
\end{aligned}
$$

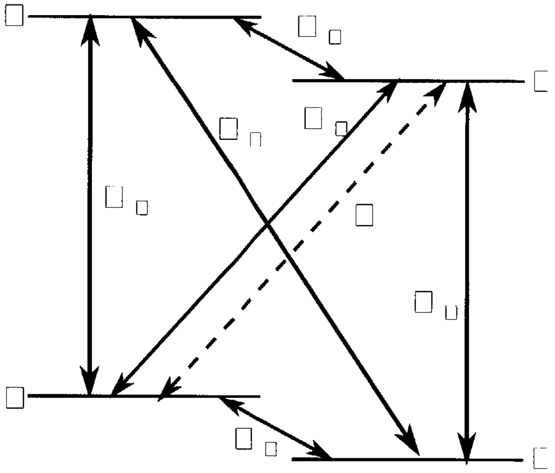

Figure 3-4: All transitions for the solid effect.

$$
\begin{aligned}
\frac{d}{dt}N_3 =& -(W+W_e+W_0+W_n)(N_3-N_3^0)\\
&+W_e(N_1-N_1^0)+(W+W_0)(N_2-N_2^0)+W_n(N_4-N_4^0)\\
\frac{d}{dt}N_4 =& -(W+W_e+W_2+W_n)(N_4-N_4^0)\\
&+W_2(N_1-N_1^0)+(W_e)(N_2-N_2^0)+W_n(N_e-N_e^0)
\end{aligned}
\tag{3.20}
$$

In terms of the polarizations this is

$$
\begin{aligned}
\frac{d}{dt}P_e &= W(P_n-P_e)-(W_0+W_2+2W_e)(P_e-P_e^0)+(W_0-W_2)\\
\frac{d}{dt}P_n &= -W(P_n-P_e)-(W_2-W_0+2W_n)(P_n-P_n^0)+(W_0-W_2)(P_e-P_e^0)
\end{aligned}
\tag{3.21}
$$

In the steady state we can assume that $P_e \approx P_e^0$ due to the weak irradiation of the electron resonance. Thus, solving for P_n we find the steady state nuclear enhancement is

$$
\begin{aligned}
\varepsilon &= \frac{P_n-P_n^0}{P_n^0}\\
&= \frac{W(P_e^0-P_n^0)}{W-W_0+W_2+2W_n}\frac{1}{P_n^0}\\
&= \frac{W}{W+\sum W_n^i}\left(\frac{\gamma_e}{\gamma_n}-1\right)
\end{aligned}
\tag{3.22}
$$

Here $\sum W_n^i$ represents all relaxation processes involving the nuclear spin, i.e. the nuclear T_1 and the cross relaxation. ε will be approximately γ_e/γ_n when the microwave irradiation strongly saturates the zero quantum line and $W >> \sum W_n$. The enhancement will be negative when γ_e and γ_n have opposite signs.

3.4 Cross Effect and Thermal Mixing

Suppose the electron concentration is high, so that electron-electron interactions are large and nuclear spins may have large couplings to more than one electron spin. Now there are additional pathways of polarization transfer. The cross effect applies to the situation where there are two electrons coupled to a single nucleus, and the nuclear Zeeman energy is equal to the electron-electron dipole coupling,

$$H_{ee} = \frac{\mu_0}{4\pi}\gamma_S^2 \left(\frac{3\left(\vec{S}_1 \cdot \vec{r}\right)\left(\vec{r} \cdot \vec{S}_2\right)}{r^5} - \frac{\vec{S}_1 \cdot \vec{S}_2}{r^3} \right) \tag{3.23}$$

The three spin system has addition mixing of states due to the perturbation H_{ee}. When states with opposite nuclear spin are degenerate, mutual electron flip-flops can lead to polarization transfer. The requirement for cross effect DNP is

$$|\omega_1^e - \omega_2^e| = \omega_n \tag{3.24}$$

Recent work in CE-DNP has been to engineer organic biradicals that satisfy this condition. ([38])

Thermal mixing describes polarization transfer in a system with many electrons and few nuclei. The dynamics are more complicated in such a system, and polarization enhancement can be described using thermodynamic arguments. We can assign a spin temperature related to the thermal equilibrium populations of each spin system using the Boltzmann distribution,

$$p = e^{-H/k_b T} \approx 1 - \frac{H}{k_b T} \tag{3.25}$$

In the rotating frame this becomes

$$\widetilde{p} = e^{\widetilde{H}/k_bT} \approx 1 - \beta_e E_e - \beta' E' \tag{3.26}$$

where β_e is the effective temperature of the electron spin bath, and β' is the temperature of the remaining terms in the Hamiltonian including nuclear Zeeman, hyperfine and dipolar couplings. The electron Zeeman, nuclear Zeeman, and remaining coupling terms in the Hamiltonian each form a spin bath. When microwave irradiation is applied, the electron spins are depolarized and the electron spin temperature increases. Because the electron spin bath is thermodynamically coupled to the nuclear spin bath, the increase in electron temperature corresponds to a decrease in nuclear spin temperature (and a decrease in the temperature of the remaining bath). The result is a polarized nuclear state [3].

Chapter 4

Optimal Control Theory

4.1 Introduction

This chapter presents the basics of optimal control theory for pulse design in NMR. We need a means of finding control fields that will excite only one DNP pathway in the electron-nuclear system. This is a challenge in the electron-nuclear system discussed here as the hyperfine interaction is on the same order as the nuclear Zeeman interaction resulting in an overlap of the zero quantum and double quantum transitions with the two electron resonances. It is difficult to irradiate the two electron resonances without exciting either of the other transitions. The problem of selective excitation is an old one in magnetic resonance, and so we begin with an introduction to control techniques in NMR.

Consider a molecule with several like nuclei at different positions. All of the nuclei will have slightly different chemical environments and therefore slightly different Larmor frequencies. If the frequencies are hundreds of megaHertz and differ by kiloHertz, it will be hard to perform a rotation on just one spin. Another obstacle to high fidelity control is the presence of unwanted interactions, such as incoherent evolution due to field inhomogeneities.

Several solutions to these problems have been developed. Adiabatic pulses have been used for inversion pulses to improve the accuracy of the flip angle and reduce the effects of spatial inhomogeneities [17, 82]. Such pulses are performed by sweeping the rf field through resonance, adiabatically changing the direction of the effective field. This method allows one to rotate spins at all frequencies within the bandwidth of the probe regardless of variations in the transverse B_1 field.

Shaped pulses have been developed and analyzed to provide greater frequency selectivity [17]. The Fourier transform of the pulse in the time domain gives the strength and range of the frequencies excited by that pulse. The frequency profile of a hard square pulse is a *sinc* function. If the pulse is made longer, the frequency profile will narrow, but there will still be weaker excitations in the sidebands of the *sinc* function. A shaped pulse can eliminate the unwanted excitations. A Gaussian pulse, for example, will have a Gaussian power spectrum, and the selectivity can be increased by increasing the width of the pulse.

Optimal control theory offers another method of designing control pulses. Generally, an OCT pulse is a numerically optimized pulse found by setting the pulse to be a certain number of time steps, and the amplitude and phase of the control field at each time step are variables in the optimization. OCT was used in liquid state NMR in 2002 to implement precise unitaries while refocusing unwanted evolution [30]. OCT provides a means of correcting pulse errors, accounting for equipment performance, and improving coherent control. OCT pulses are capable of selectively inverting coupled spins and have been used to demonstrate quantum algorithms in liquid state NMR [62, 93], to control few qubit systems in solid state NMR [7], and for refocusing sequences in pulsed ESR [11].

There are several algorithms for finding optimal control pulses. These include strongly modulated pulses, which are designed to drive the system with periods of free evolution alternating with periods of strong control. Pulses designed using GRadient Ascent Pulse Engineering (GRAPE) algorithm are often used in NMR to efficiently find optimal control parameters [79]. Sequential update algorithms based on Krotov methods may offer speed ups over graident ascent methods for large dimensional systems as they do not require the computation of gradients [54, 92]. The Chopped RAndomized Basis (CRAB) algorithm which optimizes a random basis of control functions to perform a desired control operation. The CRAB algorithm has been shown to be useful for control in quantum many body problems [27]. There are also many variations on these methods to include open quantum system dynamics or experimental limitations on the control [92, 56, 10]. In this chapter we will discuss two of these methods: strongly modulated pulses and pulse finding using the GRAPE algorithm.

4.2 Strongly Modulated Pulses

The basic idea of coherent quantum control with OCT is to numerically optimize a sequence of many short pulses to produce a composite pulse which performs the desired evolution with high fidelity. In NMR (or ESR) the control Hamiltonian is an applied RF (microwave) field. The total Hamiltonian for these spins systems is the sum of the internal Hamiltonian and the external control,

$$\begin{aligned}
H &= H_{int} + H_{ext} && (4.1)\\
H_{int} &= \frac{\mu_e}{\hbar}\sum B_0\mathbf{g}_e^i S_z^i + \frac{\mu_n}{\hbar}\sum B_0\mathbf{g}_n^j I_z^j + H_{HF} + H_{dd}^n + H_{DD}^e && (4.2)\\
H_{ext}^e &= \sum_i e^{-i(\omega_{\mu w}t+\phi)tS_z^i}(-i\omega_s S_z^i)e^{+i(\omega_{\mu w}t+\phi)tS_z^i} && (4.3)\\
H_{ext}^n &= \sum_i e^{-i(\omega_{RF}t+\phi)tI_z^j}(-i\omega_I I_z^j)e^{+i(\omega_{RF}t+\phi)tI_z^j} && (4.4)
\end{aligned}$$

The goal of the pulse finder is to find the unitaries for each step defined by H_{ext} and the control parameters which produce a total unitary close to the desired evolution. One common choice for the optimization algorithm (and the choice used in later chapters here) is the Nelder-Mead simplex method. This method is a nonlinear search used to optimize many parameters simultaneously when they have inter-dependencies.

The metric for the optimization is the overlap of the unitary operator that the composite pulse performs with the desired unitary. One choice for this metric is the Hilbert-Schmidt fidelity [30],

$$\Phi = \left|tr(U_{goal}^{\dagger}U_{pulse})\right|^2/N^2 \qquad (4.5)$$

which measures how close the pulse rotation is to the desired evolution. The pulse is composed of many short, square pulses. The pulse unitary will be the composition of the unitaries for each time step,

$$U_{pulse} = U_{t_1} U_{t_2} \cdots U_{t_n} \tag{4.6}$$

Strongly modulated (SM) pulses have been used to selectively excite spins distinguished only by a chemical shift term in the internal Hamiltonian [30, 70]. We use SM pulses in this work to transfer polarization through only one pathway without exciting transitions that lead to polarization transfer in the opposite direction. SM pulses achieve the desired control by allowing periods of free evolution and periods of controlled evolution with the microwave field is on. The control Hamiltonian must be strong enough to prevent errors and suppress unwanted evolution. In other words, the microwave amplitude must be larger than the interactions that are suppressed.

In addition to unitary errors, OCT pulses found with this method are also robust against incoherent errors. Such errors can occur due to field inhomogeneities in the external B_0 field or the small B_1 rf field. These nonuniformities in the field induce variations in the Larmor frequencies of the spins in the sample. SM pulses can refocus errors due to these variations while performing the intended rotation.

SM pulses have been used in liquid state NMR systems with up to 12 qubits. The ability to selectively excite spins at frequencies only tens of Hertz apart is essential for quantum processing with a large number of qubits in NMR. OCT pulses were used to generate 12-spin coherence and a 12-spin pseudo-pure state [62].

4.2.1 Open Systems

A pulse finder for SM pulses finds the unitary for each time step and calculates the overall evolution of the pulses, it is straightforward to adapt this to a superoperator picture for an open system optimization. In the case when nonunitary evolution is a significant source of error, we have to consider open system dynamics. Thus we modify the optimization metric by using the gate fidelity defined as [30, 64],

$$F = \overline{C(\rho_{goal}\rho_{pulse})} \tag{4.7}$$

where ρ_{goal} is the ideal final state if only unitary evolution were present, ρ_{pulse} is the state resulting from the pulse implemented and including both unitary evolution and decoherence. $C(\cdot,\cdot)$ is the attenuated correlation function of the two states, ρ_{goal} and ρ_{pulse},

$$C(\rho_{goal}\rho_{pulse}) = \frac{tr(\rho_{goal}\rho_{pulse})}{\sqrt{tr(\rho_{goal}^2)tr(\rho_{pulse}^2)}} \tag{4.8}$$

and the average, $\overline{C}$, is the average over a complete set of initial states.

The map for taking the initial state ρ to ρ_{goal} is fully determined by U_{goal} while the map for ρ_{pulse} can be represented by a Kraus decomposition [64, 30]:

$$\rho_{goal} = U_{goal}\rho U_{goal}^{\dagger}, \qquad \rho_{pulse} = \sum_k A_k \rho A_k^{\dagger} \tag{4.9}$$

Plugging this into Eq. 4.7, the gate fidelity reduces to

$$F = \sum_k \left| Tr(U_{goal}^{\dagger}A_k)/N \right|^2 \tag{4.10}$$

4.3 Gradient Ascent Algorithms

One class of algorithms that has been used extensively in OCT pulse design is gradient ascent algorithms [44, 45, 79]. Although the experiments presented later in this work did not use such an algorithm, pulse finding using these algorithms can produce high fidelity control and is more efficient for composite pulses consisting of many time steps.

As mentioned previously, the total Hamiltonian is the sum of the internal and control Hamiltonians. In the gradient ascent pulse engineering (GRAPE) algorithm, the pulse is discretized into a number of time steps. Then the unitary operator for each time step, j, is

$$U_j = \exp\left[-i\Delta t\left(H_{\text{int}} + \sum_i u_i(j)H_j\right)\right] \tag{4.11}$$

with Δt, the length of the time step. The unitary for the total pulse is the product of the U_j. Plugging this into the performance function, Φ from Eq (4.5) gives

$$\begin{aligned}\Phi &= \left|tr\left(U_{goal}U_M\cdots U_1\right)\right|^2/N^2 && (4.12)\\ &= \left|tr\left(\left(U_{j+1}^\dagger\cdots U_M^\dagger U_{goal}\right)^\dagger U_j\cdots U_1\right)\right|^2/N^2 && (4.13)\end{aligned}$$

Eq. (4.13) is a useful form for calculating the derivatives of Φ. $U_j\cdots U_1$ is the unitary evolution due to the control pulse up to the jth time step. The term $U_{j+1}^\dagger\cdots U_M^\dagger U_{goal}$ is the goal unitary backwards propagated to the jth time step using the control pulses found for the $j+1$ to M steps. We will also need to find the derivative of U_j with respect to the control fields $u_i(j)$ for each step,

$$\frac{\delta U_j}{\delta u_i(j)} \approx -i\Delta t H_i U_j \tag{4.14}$$

under the condition $\Delta t H \ll 1$. The next step is to calculate the derivative of the fidelity given in Eq. 4.5,

$$\frac{\delta\Phi}{\delta u_i(j)} = \frac{1}{N^2}\left[tr\left(\left(U_{j+1}^\dagger\cdots U_M^\dagger U_{goal}\right)^\dagger \frac{\delta U_j}{\delta u_i(j)}U_{j-1}\cdots U_1\right) + c.c.\right] \tag{4.15}$$

Φ is improved if the control parameters are updated using these derivatives,

$$u_i(j) \rightarrow u_i(j) + \epsilon\frac{\delta\Phi_0}{\delta u_i(j)} \tag{4.16}$$

The GRAPE algorithm provides a more efficient means of finding control parameters than other numerical optimizations as the gradient indicates in which direction the control parameters should be changed. The basic algorithm as first presented in [45] is as follows,

1. Guess initial parameters.

2. Calculate the state for each time step by applying U_j given $u_i(j)$ from (1)

3. Calculate the goal operator backwards propagated to each step, $U_{j+1}^{\dagger} \cdots U_M^{\dagger} U_{goal}$

4. Evaluate the gradient of the fidelity and update the control parameters.

5. Return to (2)

As with other methods of pulse optimization, it is possible for the GRAPE algorithm to find pulses which are a local minimum instead of a global minimum, but this algorithm does provide significant improvement in pulse design over other methods. Calculating the gradients is more efficient than evolving the state through each time step for one iteration of pulse optimization. Studies of the control landscapes for these optimization problems have demonstrated that the solutions are often nearly optimal [59, 67]. In particular, for the case of control with no constraints, any extrema in the control landscape will correspond to either global optimal control or to no control [74].

It is important that the internal and control Hamiltonians are well known in order to successfully implement GRAPE pulses. If the system Hamiltonian is not well known, GRAPE is not a good optimization procedure. Even when the system is well described, an educated guess of the initial parameters can improve the performance of the algorithm.

4.3.1 Open Systems

To include relaxation in pulse optimization one can use a Lindbladian (as described in Chapter 2 to represent the superoperator. In the GRAPE algorithm the Lindbladian simply replaces the unitary operators[45]. $\mathcal{L}$ is now the generator, where $\mathcal{L}$ is

$$\mathcal{L} = -iH + \Gamma \tag{4.17}$$

where Γ is the dissipator that drives relaxation dynamics. Using the density operator representation, we can write the performance function as

$$\begin{aligned} \Phi &= tr\left(U_{goal}\rho(T)\right) && (4.18) \\ &= tr\left(L_{j+1}^{\dagger}\cdots L_{M}^{\dagger}U_{goal}L_{1}\cdots L_{j}\rho_{0}\right) && (4.19) \end{aligned}$$

with

$$L_j = e^{-\mathcal{L}\Delta t} \tag{4.20}$$

and

$$\rho(T) = L_N \cdots L_1 \rho_0 \tag{4.21}$$

Chapter 5

Pulse Finding and Simulation

The system of interest is one electron hyperfine coupled to one proton. In this two spin case there are two mechanisms of dynamic nuclear polarization: the solid effect and the Overhauser effect. The solid effect transfers polarization through direct irradiation of the zero quantum transition, inducing an electron-nucleus flip flop[3]. The Overhauser effect indirectly causes this flip flop through a relaxation process that occurs when the electron resonances are saturated[66]. Both of these processes depend on the zero quantum states being mixed through an anisotropic hyperfine coupling. Without this mixing the zero quantum transition is a forbidden transition, and there is no cross relaxation.

As mentioned in Chapter 3, the theoretical nuclear polarization enhancement is limited by the ratio γ_e/γ_n [40]. For protons, the maximum achievable enhancement is 660. In any physical system the enhancement will be less than the theoretical limit due to a number of factors, such as asymmetric saturation of the electron resonances, leakage due to nuclear relaxation or double quantum transitions, and most importantly the competition between various DNP processes. The solid effect and Overhauser effect occur simultaneously when a microwave field is applied, but they yield nuclear polarization enhancements of opposite sign. Consequently the net polarization enhancement is reduced. It is advantageous to find a control sequence that allows one DNP process while the other is suppressed. A pulse sequence capable of selecting one of these two opposing methods of DNP must account for decoherent

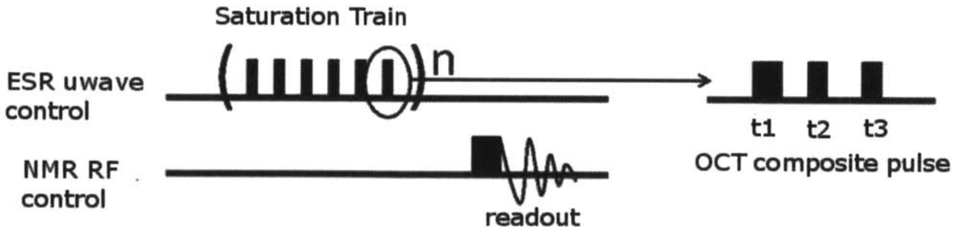

Figure 5-1: Timing diagram of the experiment: the $\pi/2$ saturation is applied for a variable length of time followed by the NMR readout pulse.

processes as well as unitary evolution.

In order to transfer polarization to the nuclear spins via the Overhauser effect, the electron resonances must be saturated (as shown in Fig. 3-1). This can be done with CW irradiation at the electron Larmor frequency, however for the purpose of comparing strongly modulating pulses to hard pulses we accomplish the electron saturation through a $\pi/2$ pulse train as shown in Figure 5-1. We will compare the results of DNP using hard pulses versus OCT pulses in this saturation train.

The pulse optimization used the Nelder-Mead simplex algorithm to search for the control parameters [63]. The pulses are restricted to on/off modulation; the total pulse consists of several time steps during which the microwave control is either on or off and the lengths of each step are left as parameters. The total pulse length is on the order of 100-200 ns.

We found two sets of OCT pulses: one including the electron T_1 and electron-nuclear T_x relaxation processes, and one considering only unitary evolution. For the open system dynamics required for DNP, these two relaxation processes are sufficient. One could also include T_2 processes or relaxation of the nuclei, but T_2 relaxation will not affect the polarization and nuclear T_1 is long compared to T_1 of the electron and therefore not necessary for designing control sequences. We use a Kraus operator representation of the superoperator to describe evolution under the control Hamiltonian with dissipative processes[65].

5.1 The System Hamiltonian

In order to design control sequences for malonic acid for DNP, we need to determine the superoperator that describes the internal and external Hamiltonians as well as the relaxation processes. The model system used for DNP is that described in the previous section: an unpaired electron in malonic acid hyperfine coupled to a nearby hydrogen nucleus on the center carbon. The Hamiltonian for this system is that given in Eq. 1.21. The anisotropic hyperfine term BI_xS_z mixes the nuclear states. S_z, the projection of the electron spin along $\hat{z}$ is still a good quantum number, but I_z is not. The energy eigenstates are,

$$\begin{aligned}
|\uparrow\alpha\rangle &= |\uparrow\Downarrow\rangle + \frac{\left(A + -\frac{1}{2}\omega_I + \sqrt{A^2 + B^2 - A\omega_I + 0.25\omega_I^2}\right)}{B}|\uparrow\Uparrow\rangle \\
|\uparrow\alpha^{\perp}\rangle &= |\uparrow\Downarrow\rangle + \frac{\left(A + -\frac{1}{2}\omega_I - \sqrt{A^2 + B^2 - A\omega_I + 0.25\omega_I^2}\right)}{B}|\uparrow\Uparrow\rangle \\
|\downarrow\beta\rangle &= |\downarrow\Uparrow\rangle - \frac{\left(-A + -\frac{1}{2}\omega_I + \sqrt{A^2 + B^2 + A\omega_I + 0.25w\omega_I^2}\right)}{B}|\downarrow\Downarrow\rangle \\
|\uparrow\beta^{\perp}\rangle &= |\downarrow\Uparrow\rangle - \frac{\left(-A + -\frac{1}{2}\omega_I - \sqrt{A^2 + B^2 + A\omega_I + 0.25\omega_I^2}\right)}{B}|\downarrow\Downarrow\rangle \qquad (5.1)
\end{aligned}$$

The parameters for this Hamiltonian under the conditions to be used in the experiment (3.4kG, orientated maximize B) are

$$\begin{aligned}
\omega_S &= -9.6\text{GHz} \\
\omega_I &= 14.6\text{MHz} \\
A &= -42.7\text{MHz} \\
B &= 14\text{MHz}
\end{aligned}$$

The control Hamiltonian describes a microwave field oscillating in the x-y plane. in order to remove the time dependence from the control Hamiltonian, we transform the internal Hamiltonian to the rotating frame of the electron spin. The microwave pulse in this frame corresponds to

$$H_{\mu w} = \omega_1 S_x \otimes \mathbb{1}_I$$

This assumes that the microwave pulse is on resonance with the electron Larmor frequency.

The relaxation processes can be represented in the Kraus operator formalism. The dominant processes are the electron T_1 and the zero quantum cross relaxation.

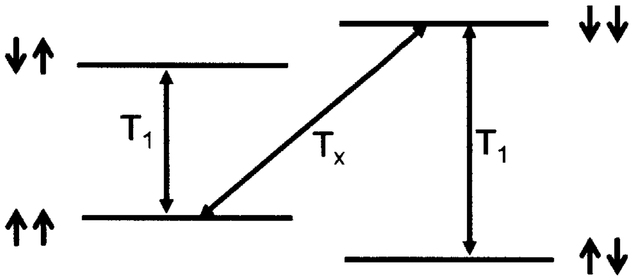

Figure 5-2: Energy levels and relaxation in the electron-nuclear hyperfine coupled system of a malonic acid radical.

5.2 Kraus Operators

5.2.1 Electron T_1

During T_1 relaxation of the electron, the electron spin flips while the nuclear spin remains in the same Zeeman state. Because I_z is not a good quantum number, the eigenstate of the nuclear spin changes, i.e. $|\uparrow \alpha\rangle \Leftrightarrow |\downarrow \beta\rangle$ and $|\uparrow \alpha^{\perp}\rangle \Leftrightarrow |\downarrow \beta^{\perp}\rangle$. A set of Kraus operators describing this type of relaxation must produce these transitions, and essentially act as the operator $S_x \otimes \mathbb{1}_I$ in the energy eigenbasis, which is given by the operator $S_x \otimes \mathbb{1}_I$. Therefore the Kraus operators for T_1 relaxation are

$$A_1 = \sqrt{1-p}\,\mathbb{I} \otimes \mathbb{I} \qquad A_2 = \sqrt{p}S_x \otimes \mathbb{I}$$

Here $p = \exp(-h\omega_S/2k_bT)$. These operators will result in a final state that has a polarization p. We actually require, however, Kraus operators that will return the system to thermal equilibrium. One set of Kraus operators which perform this process is the following:

$$\begin{array}{ll} A_1 = \sqrt{p}\begin{pmatrix} 1 & 0 \\ 0 & \sqrt{\epsilon} \end{pmatrix} \otimes \mathbb{I} & A_2 = \sqrt{p}\begin{pmatrix} 0 & \sqrt{1-\epsilon} \\ 0 & 0 \end{pmatrix} \otimes \mathbb{I} \\ A_3 = \sqrt{1-p}\begin{pmatrix} \sqrt{\epsilon} & 0 \\ 0 & 1 \end{pmatrix} \otimes \mathbb{I} & A_4 = \sqrt{1-p}\begin{pmatrix} 0 & 0 \\ \sqrt{1-\epsilon} & 0 \end{pmatrix} \otimes \mathbb{I} \end{array} \tag{5.2}$$

Where $\epsilon = \exp(-t/T_1^e)$.

The other set of Kraus operators we need to include in the pulse finder is that which describes the electron-nuclear flip-flop cross relaxation. This is essentially a T_1 process that acts only on the zero quantum subspace, a depolarizing channel that leads to transitions $|\downarrow \beta\rangle \Leftrightarrow |\uparrow \alpha^{\perp}\rangle$. It is useful to define modified Pauli matrices that act on the space formed by these two states.

$$I_{ZQ} = \frac{1}{2} I \otimes I - \frac{1}{2} Z \otimes Z = \begin{pmatrix} 0 & & & \\ & 1 & & \\ & & 1 & \\ & & & 0 \end{pmatrix}$$

$$X_{ZQ} = \frac{1}{2} X \otimes X + \frac{1}{2} Y \otimes Y = \begin{pmatrix} 0 & & & \\ & 0 & 1 & \\ & 1 & 0 & \\ & & & 0 \end{pmatrix}$$

$$Y_{ZQ} = \frac{1}{2}X \otimes Y - \frac{1}{2}Y \otimes X = \begin{pmatrix} 0 & & & \\ & 0 & -i & \\ & i & 0 & \\ & & & 0 \end{pmatrix}$$

$$Z_{ZQ} = \frac{1}{2}Z \otimes I - \frac{1}{2}I \otimes Z = \begin{pmatrix} 0 & & & \\ & 1 & & \\ & & -1 & \\ & & & 0 \end{pmatrix}$$

$$I'_{ZQ} = \frac{1}{2}I \otimes XI + \frac{1}{2}Z \otimes Z = \begin{pmatrix} 1 & & & \\ & 0 & & \\ & & 0 & \\ & & & 1 \end{pmatrix} \tag{5.3}$$

For cross relaxation the Kraus operators are

$$\begin{aligned} B_1 &= \sqrt{1-3p}(I_{ZQ} + I'_{ZQ}) & B_2 &= \sqrt{p}(X_{ZQ} + I'_{ZQ}) \\ B_3 &= \sqrt{p}(Y_{ZQ} + I'_{ZQ}) & B_4 &= \sqrt{p}(Z_{ZQ} + I'_{ZQ}) \end{aligned} \tag{5.4}$$

These operators will depolarize the zero quantum subspace, but as in the electron T_1 case we actually want to return to thermal equilibrium. The correct Kraus picture is

$$B_1 = \sqrt{0.5p_{zq}} \begin{pmatrix} 1 & 0 & 0 & 0 \\ 0 & 1 & 0 & 0 \\ 0 & 0 & \sqrt{\epsilon_{zq}} & 0 \\ 0 & 0 & 0 & 1 \end{pmatrix} \qquad B_2 = \sqrt{0.5p_{zq}} \begin{pmatrix} 0 & 0 & 0 & 0 \\ 0 & 0 & \sqrt{1-\epsilon_{zq}} & 0 \\ 0 & 0 & 0 & 0 \\ 0 & 0 & 0 & 0 \end{pmatrix}$$

$$B_3 = \sqrt{1-0.5p_{zq}}\begin{pmatrix} 1 & 0 & 0 & 0 \\ 0 & \sqrt{\epsilon_{zq}} & 0 & 0 \\ 0 & 0 & 1 & 0 \\ 0 & 0 & 0 & 1 \end{pmatrix} \quad B_4 = \sqrt{1-0.5p_{zq}}\begin{pmatrix} 0 & 0 & 0 & 0 \\ 0 & 0 & 0 & 0 \\ 0 & 0 & \sqrt{1-\epsilon_{zq}} & 0 \\ 0 & 0 & 0 & 0 \end{pmatrix} \tag{5.5}$$

with $p_{zq} = \exp(-h(\omega_S - \omega_I)/2k_bT)$ and $\epsilon_{zq} = \exp(-t/T_{ZQ})$, where T_{ZQ} is the zero quantum cross relaxation. These Kraus operators satisfy the condition $\sum_k B_k^\dagger B_k = 1$. The Kraus operators for return to equilibrium for the double quantum pathway (electron-nuclear flip-flip relaxation) can be constructed similarly. These operators are

$$C_1 = \sqrt{0.5p_{dq}}\begin{pmatrix} 1 & 0 & 0 & 0 \\ 0 & 1 & 0 & 0 \\ 0 & 0 & 1 & 0 \\ 0 & 0 & 0 & \sqrt{\epsilon_{dq}} \end{pmatrix} \qquad C_2 = \sqrt{0.5p_{dq}}\begin{pmatrix} 0 & 0 & 0 & 0 \\ 0 & 0 & 0 & \sqrt{1-\epsilon_{dq}} \\ 0 & 0 & 0 & 0 \\ 0 & 0 & 0 & 0 \end{pmatrix}$$
$$C_3 = \sqrt{1-0.5p_{dq}}\begin{pmatrix} \sqrt{\epsilon_{dq}} & 0 & 0 & 0 \\ 0 & 1 & 0 & 0 \\ 0 & 0 & 1 & 0 \\ 0 & 0 & 0 & 1 \end{pmatrix} \quad C_4 = \sqrt{1-0.5p_{dq}}\begin{pmatrix} 0 & 0 & 0 & 0 \\ 0 & 0 & 0 & 0 \\ 0 & 0 & 0 & 0 \\ \sqrt{1-\epsilon_{dq}} & 0 & 0 & 0 \end{pmatrix} \tag{5.6}$$

with $p_{dq} = \exp(-h(\omega_S - \omega_I)/2k_bT)$ and $\epsilon_{dq} = \exp(-t/T_{DQ})$. T_{DQ} is the double quantum cross relaxation.

Although it is not necessary to include the nuclear relaxation for the pulse finding discussed here, we give the Kraus operators for the nuclear return to equilibrium for completeness:

$$D_1 = \sqrt{p_n}\,\mathbb{I}\otimes\begin{pmatrix} 1 & 0 \\ 0 & \sqrt{\epsilon_n} \end{pmatrix} \qquad D_2 = \sqrt{p_n}\,\mathbb{I}\otimes\begin{pmatrix} 0 & \sqrt{1-\epsilon_n} \\ 0 & 0 \end{pmatrix}$$
$$D_3 = \sqrt{1-p_n}\,\mathbb{I}\otimes\begin{pmatrix} \sqrt{\epsilon_n} & 0 \\ 0 & 1 \end{pmatrix} \qquad D_4 = \sqrt{1-p_n}\,\mathbb{I}\otimes\begin{pmatrix} 0 & 0 \\ \sqrt{1-\epsilon_n} & 0 \end{pmatrix} \tag{5.7}$$

Here $p_n = \exp(-h\omega_I/2k_bT)$ and $\epsilon_n = \exp(-t/T_1^n)$.

The superoperator contains both the unitary evolution under the internal and control Hamiltonians as well as relaxation according to the Kraus operators which describe T_1 ($\{A_k\}$) and T_x ($\{B_k\}$) processes as found above:

$$\rho' = \sum_k A_k \left[\sum_l B_l e^{-i(H_{int}+H_{ext}(t))t}\rho e^{i(H_{int}+H_{ext}(t))t} B_l^\dagger\right] A_k^\dagger \tag{5.8}$$

5.3 The Desired Unitary

In the case of DNP where the final state after polarization is not necessarily known, it is easier to find pulses which perform a desired unitary operator. The goal here is to find optimal control pulses which perform the $\pi/2$ rotation in the saturation train of Fig. 5-1 For this system we wish to find $\pi/2$ pulses which saturate the electron resonances without exciting the zero quantum transition in order to select the Overhauser effect (or vice versa to select the Solid effect). The Overhauser effect is a stronger process, so it is possible to find pulses which saturate the electron resonances only rather than to find pulses that drive the zero quantum transition only.

The desired unitary for Overhauser DNP is given by

$$U = \exp(-i\pi/2S_x \otimes \mathbb{1}_I) \tag{5.9}$$

where the operators are written in the eigenbasis of the system, and S_i acts on the electron spin and I_j on the nuclear spin.

For solid effect DNP the unitary should perform the rotation

$$U = \exp(-i\pi/2R) \tag{5.10}$$

where R performs the following rotation on the zero quantum subspace,

$$R = \begin{pmatrix} 1 & 0 & 0 & 0 \\ 0 & 0 & 1 & 0 \\ 0 & 1 & 0 & 0 \\ 0 & 0 & 0 & 1 \end{pmatrix}$$

5.4 The Fit Function

The fit function in the pulse finder should measure how close the OCT pulse is to performing the desired unitary. For an open quantum system, one must find the superoperator that describes the OCT pulse with the relaxation present in the system. We can use the following measure of fidelity,

$$F = \sum_k Tr(U^\dagger M_k)^2/2^D \tag{5.11}$$

where U is the unitary we want to perform and $\{M_k\}$ is the non-unique set of Kraus operators that describe the pulse superoperator.

It may also be useful to add penalties to the fit function to suppress unwanted transitions. For example, the solid effect is weaker than the Overhauser effect, so one can find pulses which lead to direct zero quantum transitions with higher fidelity if there is a penalty on exciting the electron resonances.

5.5 Using the Choi Matrix

The smallest set of Kraus operators, $\{M_k\}$, in Eq. (5.11) can be found from the Choi matrix of the superoperator given by the Kraus map, Eq. 5.8. In order to speed up the calculations for the pulse finding algorithm, one can derive the smallest set of Kraus operators from the Choi matrix given by the superoperator after each step. Here we give an example of finding this set by following the procedure outlined in Chapter 2.

We start by writing out Kraus operators for T_1^e and T_{ZQ} relaxation given the parameters of our physical system, and follow this by finding the Choi matrix of this map and determining the smallest set, $\{M_k\}$. In order to write the correct Kraus operators for T_1^e or T_{ZQ} processes, we need to know the Larmor frequencies and the relaxation times. For the system we simulated these values are $\omega_S = 9.36$ GHz and $\omega_I = 14.24$ MHz, and $T_1^e = 100\mu$s and $T_{ZQ} = 2T_1^e$. The time step is $t = 10\mu$s. We use the Kraus operators as defined earlier in this chapter. The set, A_k, for T_1 relaxation at room temperature looks like:

$$A_1 = \left(e^{-\frac{\hbar\omega_S}{2Tk_B}}\right)^{1/2} \begin{pmatrix} 1 & 0 \\ 0 & \sqrt{e^{-t/T_1^e}} \end{pmatrix} \otimes \mathbb{1} = \begin{pmatrix} 0.7068 & 0 & 0 & 0 \\ 0 & 0.70680 & 0 & 0 \\ 0 & 0 & 0.6724 & 0 \\ 0 & 0 & 0 & 0.6724 \end{pmatrix}$$

$$A_2 = \left(e^{-\frac{\hbar\omega_S}{2Tk_B}}\right)^{1/2} \begin{pmatrix} 0 & \sqrt{1 - e^{-t/T_1^e}} \\ 0 & 0 \end{pmatrix} \otimes \mathbb{1} = \begin{pmatrix} 0 & 0 & 0.2180 & 0 \\ 0 & 0 & 0 & 0.2180 \\ 0 & 0 & 0 & 0 \\ 0 & 0 & 0 & 0 \end{pmatrix}$$

$$A_3 = \left(1 - e^{-\frac{\hbar\omega_S}{2Tk_B}}\right)^{1/2} \begin{pmatrix} \sqrt{e^{-t/T_1^e}} & 0 \\ 0 & 1 \end{pmatrix} \otimes \mathbb{1} = \begin{pmatrix} 0.6729 & 0 & 0 & 0 \\ 0 & 0.6729 & 0 & 0 \\ 0 & 0 & 0.7074 & 0 \\ 0 & 0 & 0 & 0.7074 \end{pmatrix}$$

$$A_4 = \left(1 - e^{-\frac{\hbar\omega_S}{2Tk_B}}\right)^{1/2} \begin{pmatrix} 0 & 0 \\ \sqrt{1-e^{-t/T_1^e}} & 0 \end{pmatrix} \otimes \mathbb{1} = \begin{pmatrix} 0 & 0 & 0 & 0 \\ 0 & 0 & 0 & 0 \\ 0.2182 & 0 & 0 & 0 \\ 0 & 0.2182 & 0 & 0 \end{pmatrix} \tag{5.12}$$

Similarly, for the zero quantum relaxation,

$$\begin{gathered}
B_1 = \left(\frac{1}{2}e^{-\frac{\hbar(\omega_S-\omega_I)}{2TkB}}\right)^{1/2} \begin{pmatrix} 1 & 0 & 0 & 0 \\ 0 & 1 & 0 & 0 \\ 0 & 0 & \sqrt{e^{-t/T_{ZQ}}} & 0 \\ 0 & 0 & 0 & 1 \end{pmatrix} = \begin{pmatrix} 0.7068 & 0 & 0 & 0 \\ 0 & 0.7068 & 0 & 0 \\ 0 & 0 & 0.6894 & 0 \\ 0 & 0 & 0 & 0.7068 \end{pmatrix} \\
B_2 = \left(\frac{1}{2}e^{-\frac{\hbar(\omega_S-\omega_I)}{2TkB}}\right)^{1/2} \begin{pmatrix} 0 & 0 & 0 & 0 \\ 0 & 0 & \sqrt{1-e^{-t/T_{ZQ}}} & 0 \\ 0 & 0 & 0 & 0 \\ 0 & 0 & 0 & 0 \end{pmatrix} = \begin{pmatrix} 0 & 0 & 0 & 0 \\ 0 & 0 & 0.1561 & 0 \\ 0 & 0 & 0 & 0 \\ 0 & 0 & 0 & 0 \end{pmatrix} \\
B_3 = \left(1 - \frac{1}{2}e^{-\frac{\hbar(\omega_S-\omega_I)}{2TkB}}\right)^{1/2} \begin{pmatrix} 1 & 0 & 0 & 0 \\ 0 & \sqrt{e^{-t/T_{ZQ}}} & 0 & 0 \\ 0 & 0 & 1 & 0 \\ 0 & 0 & 0 & 1 \end{pmatrix} = \begin{pmatrix} 0.7074 & 0 & 0 & 0 \\ 0 & 0.6899 & 0 & 0 \\ 0 & 0 & 0.7074 & 0 \\ 0 & 0 & 0 & 0.7074 \end{pmatrix} \\
B_4 = \left(1 - \frac{1}{2}e^{-\frac{\hbar(\omega_S-\omega_I)}{2TkB}}\right)^{1/2} \begin{pmatrix} 0 & 0 & 0 & 0 \\ 0 & 0 & 0 & 0 \\ 0 & 0 & \sqrt{1-e^{-t/T_{ZQ}}} & 0 \\ 0 & 0 & 0 & 0 \end{pmatrix} = \begin{pmatrix} 0 & 0 & 0 & 0 \\ 0 & 0 & 0 & 0 \\ 0 & 0.1562 & 0 & 0 \\ 0 & 0 & 0 & 0 \end{pmatrix}
\end{gathered} \tag{5.13}$$

We now construct the Choi matrix according to Eq. (2.13) by applying the map,

$$\sum_n A_n \sum_m B_m(\cdot)B_m^\dagger A_n^\dagger \tag{5.14}$$

to the E_{ij}. The Choi matrix for the map created by these two sets of Kraus operators is

$$\begin{pmatrix}
0.9524 & 0 & 0 & 0 & 0 & 0.9406 & 0 & 0 & 0 & 0 & 0.9395 & 0 & 0 & 0 & 0 & 0.9512 \\
0 & 0.0012 & 0 & 0 & 0 & 0 & 0 & 0 & 0 & 0 & 0 & 0 & 0 & 0 & 0 & 0 \\
0 & 0 & 0.0465 & 0 & 0 & 0 & 0 & 0.0470 & 0 & 0 & 0 & 0 & 0 & 0 & 0 & 0 \\
0 & 0 & 0 & 0 & 0 & 0 & 0 & 0 & 0 & 0 & 0 & 0 & 0 & 0 & 0 & 0 \\
0 & 0 & 0 & 0 & 0 & 0 & 0 & 0 & 0 & 0 & 0 & 0 & 0 & 0 & 0 & 0 \\
0.9406 & 0 & 0 & 0 & 0 & 0.9291 & 0 & 0 & 0 & 0 & 0.9277 & 0 & 0 & 0 & 0 & 0.9395 \\
0 & 0 & 0 & 0 & 0 & 0 & 0.0232 & 0 & 0 & 0 & 0 & 0 & 0 & 0 & 0 & 0 \\
0 & 0 & 0.0470 & 0 & 0 & 0 & 0 & 0.0476 & 0 & 0 & 0 & 0 & 0 & 0 & 0 & 0 \\
0 & 0 & 0 & 0 & 0 & 0 & 0 & 0 & 0.0475 & 0 & 0 & 0 & 0 & 0.0470 & 0 & 0 \\
0 & 0 & 0 & 0 & 0 & 0 & 0 & 0 & 0 & 0.0232 & 0 & 0 & 0 & 0 & 0 & 0 \\
0.9395 & 0 & 0 & 0 & 0 & 0.9277 & 0 & 0 & 0 & 0 & 0.9292 & 0 & 0 & 0 & 0 & 0.9407 \\
0 & 0 & 0 & 0 & 0 & 0 & 0 & 0 & 0 & 0 & 0 & 0 & 0 & 0 & 0 & 0 \\
0 & 0 & 0 & 0 & 0 & 0 & 0 & 0 & 0 & 0 & 0 & 0 & 0 & 0 & 0 & 0 \\
0 & 0 & 0 & 0 & 0 & 0 & 0 & 0 & 0.0470 & 0 & 0 & 0 & 0 & 0.0464 & 0 & 0 \\
0 & 0 & 0 & 0 & 0 & 0 & 0 & 0 & 0 & 0 & 0 & 0 & 0 & 0 & 0.0012 & 0 \\
0.9512 & 0 & 0 & 0 & 0 & 0.9395 & 0 & 0 & 0 & 0 & 0.9407 & 0 & 0 & 0 & 0 & 0.9525
\end{pmatrix} \tag{5.15}$$

The last step is to construct a single set of Kraus operators from the normalized eigenvalues of the Choi matrix. For example, the eigenvector with the largest eigenvalue (which is equal to 3.76) is

$$|a\rangle = \begin{pmatrix} 0.1258 \\ 0 \\ 0 \\ 0 \\ 0 \\ 0.1242 \\ 0 \\ 0 \\ 0 \\ 0 \\ 0.1242 \\ 0 \\ 0 \\ 0 \\ 0 \\ 0.1258 \end{pmatrix}$$

Finally we normalize this and reshape the vector into a 4 × 4 matrix to make one

Kraus operator:

$$M_1 = \sqrt{16}\sqrt{3.76}\begin{pmatrix} 0.1258 & 0 & 0 & 0 \\ 0 & 0.1242 & 0 & 0 \\ 0 & 0 & 0.1242 & 0 \\ 0 & 0 & 0 & 0.1258 \end{pmatrix} = \begin{pmatrix} 0.9756 & 0 & 0 & 0 \\ 0 & 0.9635 & 0 & 0 \\ 0 & 0 & 0.9636 & 0 \\ 0 & 0 & 0 & 0.9756 \end{pmatrix}$$

We would repeat this process for all eigenvectors of the Choi matrix to obtain the full set of 16 Kraus operators. The smallest set will always have d^2 elements, with d the dimension of the Hilbert space.

In this example of only two relaxation processes this procedure does not offer much computation advantage since we could expand the sum in Eq. (5.14) into products of the form $A_m B_n$. There are 16 of these products, so using the Choi matrix does not produce a smaller set of operators. If we add a third process (such as the action of the pulse), this procedure will reduce the number of Kraus operators from 64 to 16, a significant improvement for shortening the computational time.

5.6 The Pulses

We used three sets of pulses in the experiment: hard pulses, strongly modulated OCT pulses designed without relaxation, and SM pulses that include relaxation effects. The hard pulses are 32 ns long for a Rabi frequency of 8 MHz. The hard pulse has a rather poor fidelity as defined by Eq. (5.11) with the desired unitary of 0.01.

The pulses found with optimal control but without including relaxation consist of two pulses with a delay between them:

$$(\tau_1) - (p_1) - (\tau_2) - (p_2) - (\tau_3) \tag{5.16}$$

$\tau_1 = 15$ ns $p_1 = 20$ ns

$\tau_2 = 25$ ns $p_2 = 26$ ns

$\tau_3 = 57$ ns

This composite pulse, which was found neglecting relaxation, has a fidelity with the desired unitary of 0.56.

The final OCT pulse found accounts for the relaxation processes and consists of three square pulses with delays as follows:

$$(\tau_1) - (p_1) - (\tau_2) - (p_2) - (\tau_3) - (p_4) - (\tau_4) \tag{5.17}$$

$\tau_1 = 15$ ns $p_1 = 20$ ns

$\tau_2 = 20$ ns $p_2 = 28$ ns

$\tau_3 = 12$ ns $p_3 = 16$ ns

$\tau_4 = 26$ ns

The fidelity for this pulse is 0.74. It appears the additional square pulses in the OCT sequences correct errors that the hard pulses allow. In the implementation of these pulses the initial and final delays are included in the delay between effective $\pi/2$ pulses in the saturation train.

We can also analyze the superoperator for the complete saturation train (i.e. the superoperator for n iterations of the $\pi/2$ pulse and delay) and compare the superoperator for each pulse to the ideal superoperator if the pulse performed goal unitary in Eq. (5.9). For all of the pulses - OCT and non-OCT - the superoperator is essentially a polarizing channel on the nuclear spin. This map takes the identity state to a polarized state as follows,

$$\Lambda(\mathbb{1}) = \mathbb{1} + pZ \tag{5.18}$$

In the ideal case p is 7.1×10^{-4}. This corresponds to the final nuclear polarization if the control pulse is the desired unitary. For the non-ideal pulses the polarizing channel has $p = 5.9 \times 10^{-5}$ for hard pulses, $p = 3.3 \times 10^{-4}$ for closed system OCT pulses, and $p = 6.2 \times 10^{-5}$ for open system OCT pulses. As we will discuss in the follow simulation section, these values of p determine the final nuclear polarization for each type of pulse.

Additionally the non-ideal unitary pulses lead to non-zero coherences, i.e. the superoperator increases σ_x contributions to the density matrix. These components for the super operator are small (less that 0.1% of p for the polarizing terms) but are interesting to note because the ideal unitary does not create any coherence on the nuclear spin.

We can also consider the effect of the saturation train on the electron spin. In all cases, the superoperator is a weak depolarizing channel:

$$\Lambda(\rho) = p\rho + \frac{1-p}{2}\mathbb{1}$$

The ideal unitary pulse depolarizes the electron by a factor of 19.7, whereas the open system OCT, closed system OCT, and hard pulses reduce the electronic polarization by factors of 6.1, 1.8, and 1.0 for respectively. The depolarizing channel for the saturation train for each of these pulses is due to the fact that the electron T_1 relaxation re-polarizes the electron spin during the delay times. The open system OCT pulses most successfully saturate the electron spin, but do not perform as well as the ideal unitary rotation. It appears that the microwave control with frequency equal to the uncoupled electron resonance ω_S does not fully drive both electron transitions in the hyperfine coupled system. However the superoperators do not indicate an asymmetric excitation of the electron transitions.

Any terms in the superoperator that drive two spin processes ($S_i I_j$ terms) are negligible for all pulses. The superoperators are primarily polarizing channels on the nuclear spin, and the final polarization is directly related to the parameter p in Eq. (5.18).

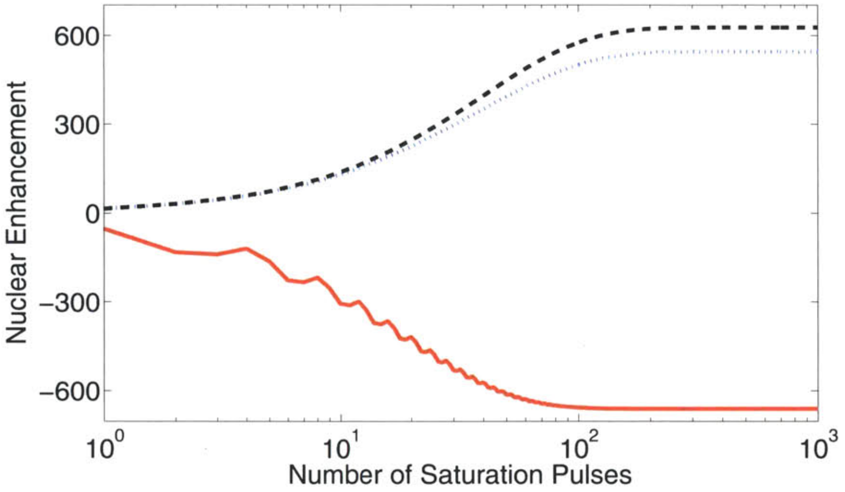

Figure 5-3: Simulation of the Overhauser effect versus the solid effect. The dashed black line is the Overhauser effect only, solid red is the solid effect only, and the blue dotted line is the result of saturation by OCT pulses.

5.7 Simulating the Pulses

After finding the optimal control pulse sequences using the methods outlined in the previous section, we simulated the system dynamics after applying the $\pi/2$ pulse train with both OCT and non-OCT pulses. For comparison, we also simulated the results of DNP if only the Overhauser effect or only the solid effect were present. Figure 5-3 compares the nuclear enhancement if only one of the DNP processes were present in the system. To simulate the Overhauser effect in the absence of the solid effect, we applied the unitary in Eq. 5.9 and a relaxation superoperator allowing for cross relation. For the case of the solid effect we applied the unitary found in Eq. 5.10 and a relaxation superoperator that did not allow for cross relaxation.

Figure 5-4 shows the results of simulating the OCT and non-OCT pulses. It should be noted that there is a significant difference between the simulated system and the physical system. In the simulations we are looking only at the two spin system described previously and find the DNP enhancement of the coupled proton. In the experiment, however, we observe the bulk proton signal, as the number of protons coupled to an electron is too small to detect directly. While the simulations do show

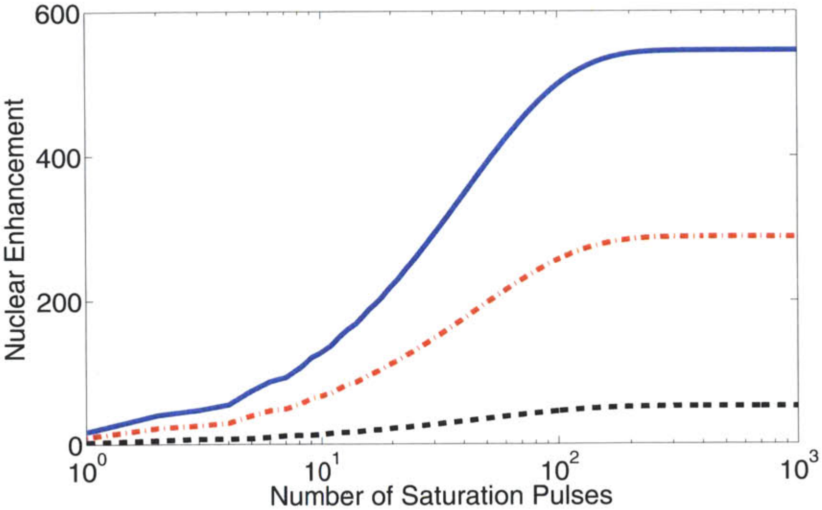

Figure 5-4: Comparison of OCT pulses to hard pulses. Blue solid line is saturation by open system OCT pulses, dashed red is closed system OCT pulses, and dashed black is saturation with hard pulses.

the relative enhancements produced by the three sets of pulses, the actual nuclear polarization depends on the couplings between the bulk protons and the hyperfine coupled protons, and the buildup times are limited by spin diffusion[75].

There are three sets of simulated data which give the nuclear enhancement after the DNP experiment using open system OCT pulse, closed system OCT pulses (no relaxation included in the pulse finder), and hard pulses (non-OCT). The simulations show that both sets of OCT pulses give a greater enhancement than hard $\pi/2$ pulses. The open system OCT pulses yield a nuclear polarization 10.5 times the hard pulse polarization and 1.9 times the closed system OCT pulses. The closed system OCT pulses produce a nuclear polarization 5.5 times that of the hard pulses.

We simulated the performance of the open system OCT pulse with variations in both Rabi frequency and the anisotropic hyperfine coupling (see Fig. 5-5). This pulse was optimized for a Rabi frequency of 8 MHz, the frequency achievable experimentally at a reasonable power. The simulations show, however, that the maximum enhancement for the OCT pulse occurs when $\omega_{Rabi} = 11$ MHz. This indicates that the higher frequency is better able to modulate the hyperfine coupling, which is set to 14 MHz. Simulations of the polarization enhancement varying the anisotropic hyperfine frequency confirm this - the optimum enhancement for $\omega_{Rabi} = 8$ MHz is closer to 10 MHz, while for the case $\omega_{Rabi} = 11$ MHz the maximum anisotropic hyperfine, 14 MHz, produces the best results.

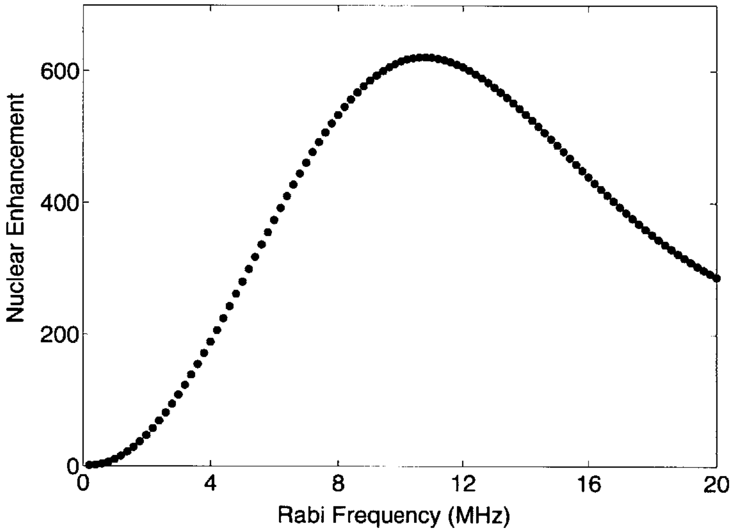

(a) Variations in Rabi frequency

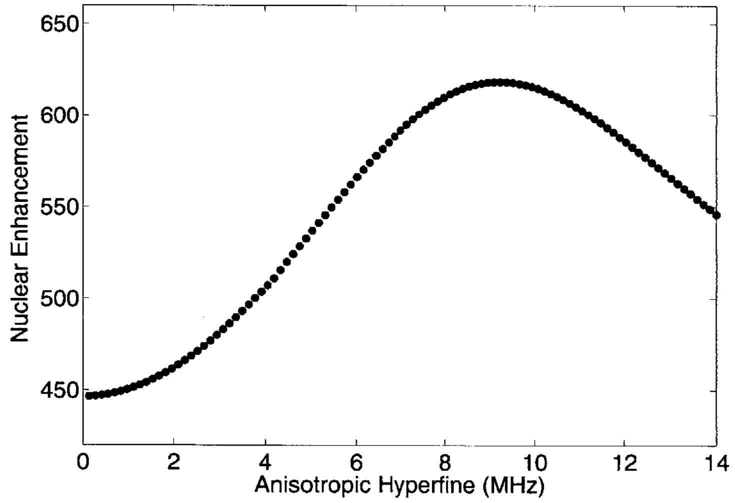

(b) Variations in anisotropic hyperfine coupling

Figure 5-5: Simulations of pulses with varying parameters.

5.7.1 Leakage Pathways

So far these simulations have shown only the idealized case of one electron and one nucleus with perfect alignment of the hyperfine coupling and perfect microwave irradiation. There are several reasons why the enhancement could be less than these predictions in the experiments. The first point to consider is that these simulations have so far neglected the double quantum pathway. While relaxation through flip-flip interactions will be a weaker process than the flip-flop that drives DNP, both pathways are present. We have simulated DNP in a system with a double quantum relaxation rate of 0.5 and 0.1 times the zero quantum rate. The results are shown in Fig 5-6. Fig. 5-7 shows the DNP enhancement of OCT versus hard pulses when the double quantum rate is half of the zero quantum transition rate. The ratios of the polarization for OCT pulses to hard pulses remain the same, but the maximum enhancement is reduced from over 500 to 170.

Another possible leakage pathway is the intrinsic nuclear T_1 relaxation. Fig. 5-8 compares the nuclear polarization enhancement for several values of T_1^n. This process does not affect the enhancement unless T_1^n is on the order of milliseconds or less. In the experimental system discussed here, T_1^n is minutes, and so we do not consider nuclear T_1 to be a significant source of leakage.

We also have to consider the spin diffusion process. The OCT pulses optimize the transfer of polarization from the electron to the proton directly coupled to it. There will be other nuclei near the defect which have some small dipolar coupling to the electron. The nuclei even further away are polarized through spin diffusion only. This spin diffusion depends on the dipole-dipole coupling between the protons.

5.8 Extension to General Case

This approach can be adapted to other open quantum systems, to include more spins or additional relaxation processes. The computations may be limited numerically by the fact that one must find operators in Liouville space as opposed to the smaller Hilbert space problems of closed system dynamics.

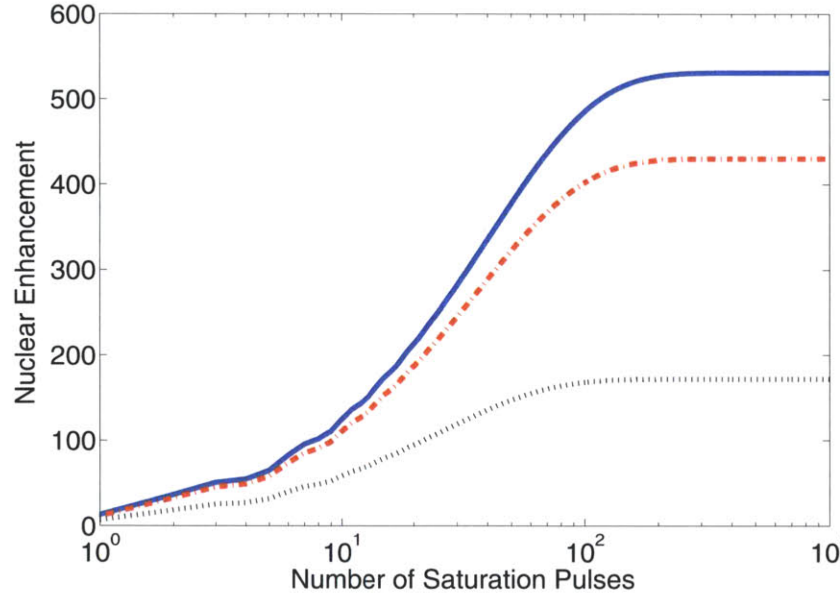

Figure 5-6: DNP with double quantum relaxation. The blue solid line is without double quantum relaxation, red dashed is with $T_{DQ} = 10T_{ZQ}$, and black dotted is with $T_{DQ} = 2T_{ZQ}$

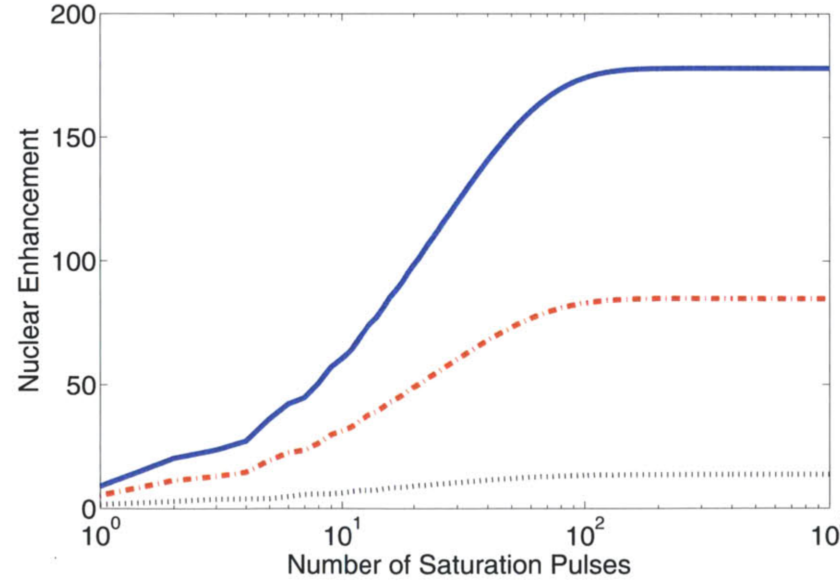

Figure 5-7: Comparison of OCT pulses versus hard with double quantum relaxation: Blue solid line is saturation by open system OCT pulses, dashed red is closed system OCT pulses, and dashed black is saturation with hard pulses.

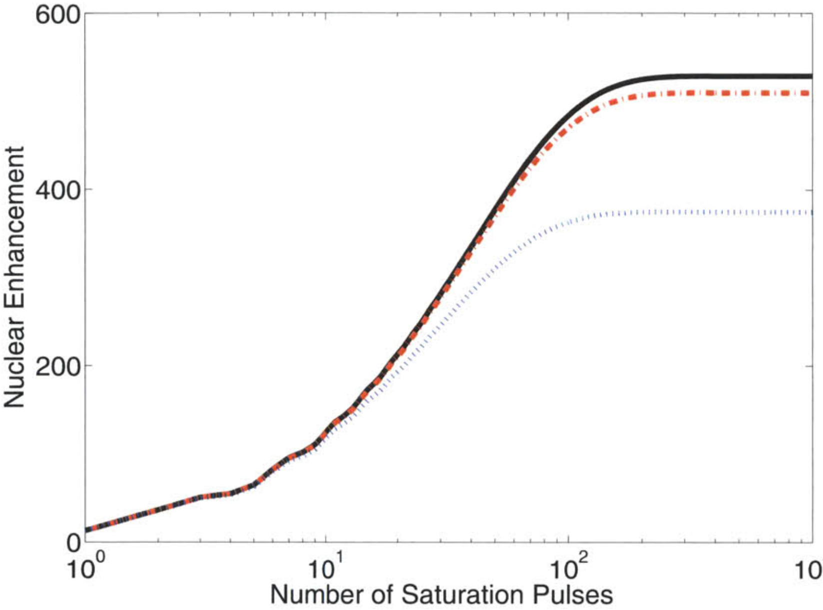

Figure 5-8: Leakage through nuclear T_1 relaxation. The solid black curve gives the enhancement when T_1^n is on the order of a minute. There is little deviation from this until T_1^n is on the order of 10 ms (red dashed), and only significant change when T_1^n is 1ms (blue dotted).

One can design control sequences that account for relaxation. The Kraus operator formalism is useful in this approach. This superoperator representation allows us to design a flexible pulse finder in which we can easily incorporate additional operators depending on the relevant processes for the system. In principle another superoperator formalism, such as the Lindblad representation under the condition that the system is Markovian, would work as well.

The inputs required are the number of steps, a starting length of the step and amplitude of the applied microwave or rf field, the internal Hamiltonian, and the relevant relaxation times. The code used above included only on/off control, but this could be expanded to include amplitude and phase control according to experimental capabilities.

Determining an appropriate fit function is necessary for finding good OCT pulses. In the case above, the overlap of the superoperator with one that performs a rotation on the electron spins is a good measure of the quality of the pulses. If one wanted instead to find pulses to select the solid effect, a weaker process, and suppress the

Overhauser effect, a fit function that measures the overlap with a rotation on the zero quantum states might not be good enough. To find better pulses, one can add a penalty function which minimizes the overlap with the unwanted operation, a rotation on the electron spin manifold in this example.

Here we used a process fidelity in the fit function, but for optimizing pulses where the desired final state is known one could use a state-to-state fidelity. In the DNP example, there are two processes with which to compare the pulses. If one wanted to perform a 2 spin gate such as a SWAP or CNOT on an open quantum system, a state fidelity would be a more natural measure.

Chapter 6

Experiment

6.1 Methods

We used a home-built DNP probe to apply microwaves to the irradiated malonic acid sample described in Chapter 1 and detect the rf NMR signal. The pulsed ESR spectrometer transmitted microwaves at $\omega_S = 9.57$ GHz, and we detected the NMR signal of the bulk at $\omega_I = 14.57$ MHz. To measure the thermal signal without DNP, we used an Ernst angle detection with 400,000 scans. Due to the large dipolar coupling between protons in malonic acid, T_2 of the proton signal was less than the deadtime of the probe, and so we used a magic echo sequence to detect the NMR signal. The proton linewidth was 40kHz.

We ran three sets of experiments, all using the basic pulse sequence given in Figure 5-1. One data set used hard $\pi/2$ pulses in the ESR saturation train, while the other two used the OCT pulses, one open system OCT pulses and one closed. The data obtained using OCT pulses was summed over 64 scans, while the data using hard pulses was averaged over 256 scans and rescaled.

6.2 DNP Probe Design

We built a dual frequency probe for pulsed ESR excitation and NMR detection. There are various designs for electron-nuclear double resonance (ENDOR) and DNP probes at high and low fields. ENDOR and DNP experiments both require simultaneous irradiation with microwave and RF fields. At high field, one typical design uses a waveguide with a horn for transmitting microwave onto a sample held in an coil that is part of the LC circuit tuned to RF frequencies [18]. Alternative high field probes use a helix for NMR coil, which doubles as a microwave cavity for the ESR resonator[94]. At low fields corresponding to X-band ESR frequencies the most common ENDOR or DNP probes use a bridged loop-gap resonator placed inside and concentric with an NMR coil [81, 29]. We have developed a novel design for a pulsed dual frequency probe for X-band DNP.

The schematic for the probe is shown in Fig 6-1. The ESR resonator is based on the standard loop-gap resonator. Loop-gap resonators (LGR) are widely used for ESR at X-band or lower frequencies. As such resonators can be made small compared to microwave cavities and typically have lower Q, they are particularly useful for pulsed ESR. LGRs have a high filling factor and consequently produce a large B_1 with good uniformity over the sample [69, 25].

In an LGR the loop acts as an inductor and the gap as a capacitor, and together they form the resonance structure of an LC circuit. The electric and magnetic fields are confined separately in space so that the E field is strongest in the gap, and the B field in the loop. Bridged loop-gap resonators were initially developed to improve the confinement of the field within the resonator by adding a shielding outer conductor [78]. BLGRs are frequency tunable and have been used in ENDOR probes [29, 68].

We present an alternative to the BLGR based ENDOR probe with similar or better performance, which, significantly, permits a simpler construction. BLGRs require depositing thin layers of metal on quartz tubes [85], while our design can be built easily with the tools standard in any lab. We use a strip of copper foil 2-3mm wide and 100μm thick and shape it into a loop-gap configuration. This ESR resonator is soldered onto the microwave coax at one end, while the other end is open (see top view of Fig 6-1). A tuning screw on the opposite side of the shield allows tuning and matching of the ESR resonance over a 1 GHz range around 10 GHz. The frequency and Q-factor of the resonator depend on the diameter of the loop and the separation

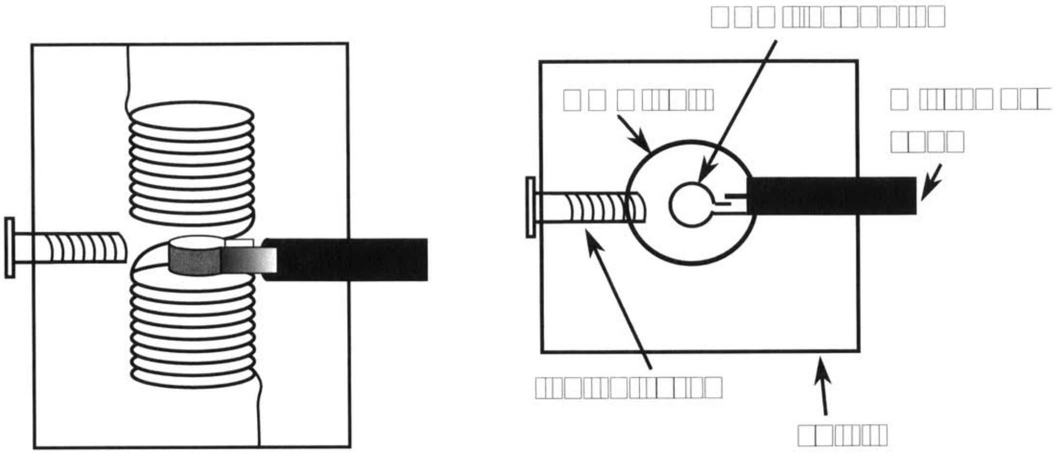

Figure 6-1: Probe Diagram: the figure on the left shows the side view of the probe, and on the right is the top view. The ESR resonator in the shape of a loop-gap is concentric to the NMR coil.

of the gap.

The ESR resonator is concentric with the NMR coil. In order to place the microwave coax and tuning screws from the side, we used a split coil design for the RF detection. In principle the coax and tuning screw could be inside the NMR coil to avoid using a split coil. In that case B_1^{RF} and $B_1^{\mu wave}$ would be perpendicular. This would improve the sensitivity of the NMR circuit, but we found the performance of the split coil to be adequate.

The NMR coil is wound on a KEL-F support (another polymer support could be used if not detecting protons). One lead is grounded to the shield, and the other is isolated from the shield and connected to the RF circuit outside the shield.

It is important to protect the microwave electronics from NMR pulses by using RF filters outside the probe. As the overlap of the microwave field and the RF field is small, there is little coupling between the two and we do not find any impact on either the ESR or NMR signal due to the presence of the other.

6.2.1 Probe Performance

The Q-factor of the ESR resonator varies depending mostly on the size of the loop. A loop with diameter 1.5mm has a Q of 100-400, while a larger loop with diameter

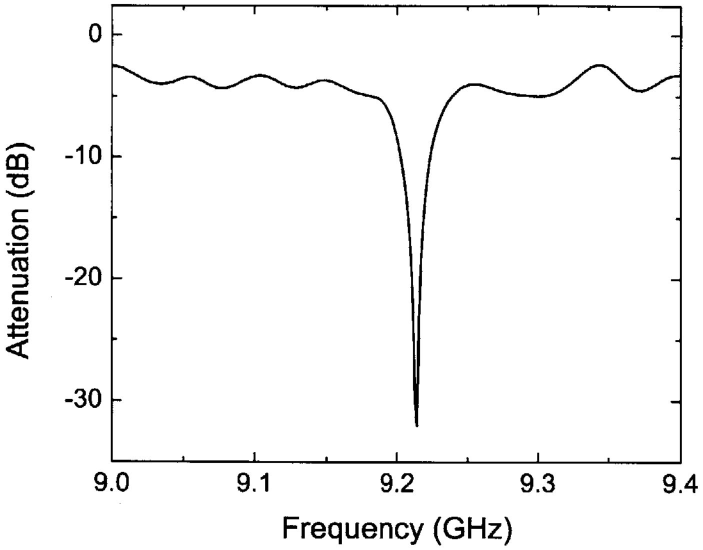

Figure 6-2: ESR resonance: this resonator is tuned to 9.21 GHz with a Q of 1000.

3mm has a Q of up to 4000. The Q can be spoiled as well using the tuning screw. Fig 6-2 plots the s11 parameter of the transfer curve for the larger resonator (loaded) while placed inside the NMR coil.

Fig 6-3 shows the FID of a sample of DPPH. In this plot we see some leakage from the pulse, but the ringdown is less than 100ns. The signal is comparable to that of a standard loop-gap resonator tuned to the same frequency. We tested the probe with the ESR resonator tuned to 10GHz and the NMR circuit tuned to 15MHz. The presence of the NMR coil does not change the Q or tuning frequency of the ESR resonator.

In order to confirm that the microwave field is confined to the loop and not an effective cavity mode of the shield, we performed a Rabi experiment on irradiated quartz. The results are given in Fig 6-4. We were able to achieve a Rabi frequency of 17MHz with 40W power using the smaller loop. The Rabi frequency decreases with a larger diameter loop as the field is not spread over a larger area. These results are the same with the NMR coil removed.

The Rabi experiment indicates that the field is fairly homogeneous within the ESR loop. Simulations of the ESR resonator confirm that field is confined to the coil

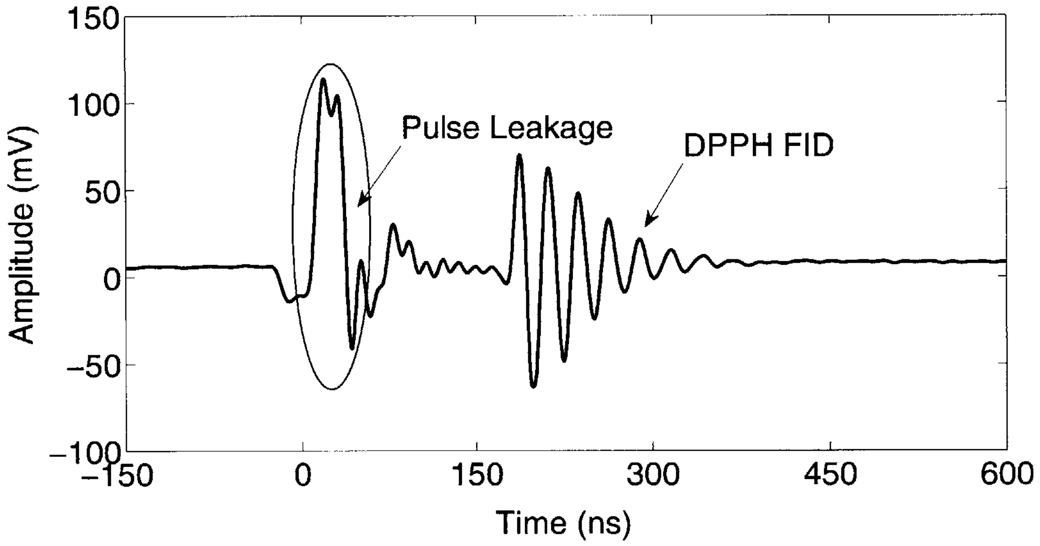

Figure 6-3: Pulsed ESR signal of DPPH with the DNP probe. We identify two main features in this figure, first the leakage of the pulse through the receiver switch. 200 ns after the pulse, the receiver switch opens we detect the DPPH free induction decay.

and is uniform over the sample (Fig 6-5).

While we have used this design for DNP experiments and detected proton signal at 15MHz, the NMR circuit could be designed for another nuclear frequency. Although the NMR coil has a low filling factor, for the DNP experiment presented here this configuration provides enough sensitivity.

This NMR/ESR dual frequency probe design is not only versatile but straightforward and simple to construct. By changing the gap size, loop diameter, and the distance of the tuning screw one can build a resonator functional at a wide range of X-band frequencies. The quality factor can be varied over a wide range, which is advantageous as many ENDOR experiments require a low Q (on the order of 100) while other pulsed ESR application may benefit from a higher Q resonator [78]. The ESR resonator itself can be used for pulsed ESR with a performance comparable to other loop-gap resonators. This probe performs similarly to bridged loop-gap ENDOR probes but can be designed and built quickly in a lab without any intensive fabrication techniques.

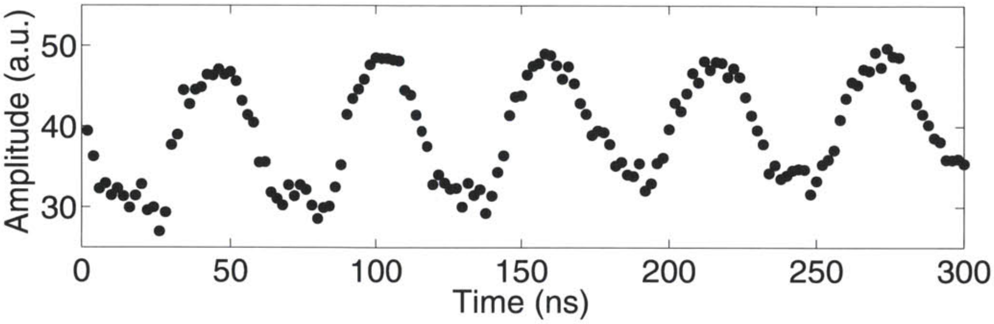

Figure 6-4: Rabi experiment with irradated quartz sample. The top plot shows the imaginary part of the signal and the lower plots shows the real part. The Rabi frequency is 17MHz.

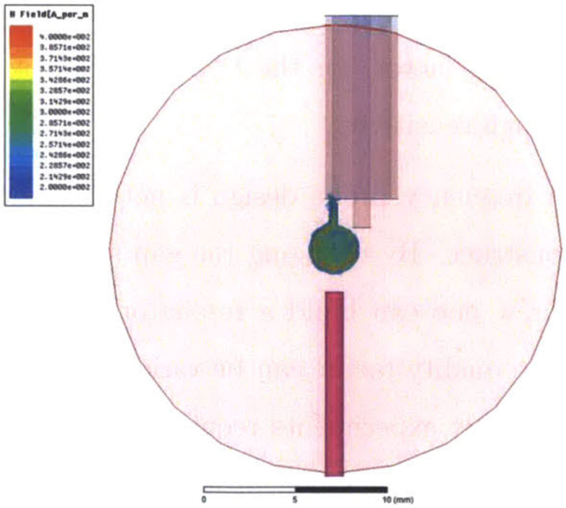

Figure 6-5: Simulation of the field homogeneity

6.3 Results

Figure 6-6 compares the NMR signals after two DNP experiments using OCT pulses: one with 1s of polarization and another with 140s polarization. Figure 6-7 shows the buildup curves for the three sets of pulses. It is clear that the OCT pulses found with relaxation processes included in the pulse finder (open system pulses) produce the highest nuclear polarization, 11.1 ± 2.2 times the enhancement produced by hard pulses, and 2.2 ± 0.4 times that produced by the OCT pulses found without relaxation (closed system pulses). The closed system pulses yield a polarization 5.1 ± 1.0 times that of hard pulses. These ratios are consistent with those found in the simulations of 5.

The maximum polarization enhancement achieved with the open OCT pulses was a factor of 180 ± 20. This is less than maximum simulated value. There are several factors which could account for this difference, however. The simulations do not include the transfer of polarization from the electron-coupled protons to the bulk protons via spin diffusion. The polarization of the bulk nuclear spin is expected to be less than the polarization of the spins coupled to protons and to depend on the strength of the proton dipole-dipole couplings [75]. There are also leakage pathways, such as the double quantum relaxation, which could reduce the overall enhancement. In fact the simulations show that a double quantum relaxation rate of half the zero quantum rate would produce results similar to those of the experiment.

From fits of the data in Figure 6-7 we find the buildup times for each curve. For all three curves the rate determining process is spin diffusion, but the buildup times will depend on how efficiently the electron coupled nuclear spins are polarized[37]. The hard $\pi/2$ pulses have a buildup time of 12.7 ± 1.8s , the closed OCT buildup is 14.9 ± 1.7s, and 13.2 ± 1.5s for the open OCT pulses.

We also measured the effective T_1 of the bulk nuclear spins after DNP. This result is shown in Figure 6-8. A fit of this curve gives $T_1 = 10.5 \pm 1.6$ s. Like the DNP process, the return to thermal equilibrium depends on spin diffusion. The fast electron T_1 process will depolarize nuclear spins in its vicinity, and that depolarization will

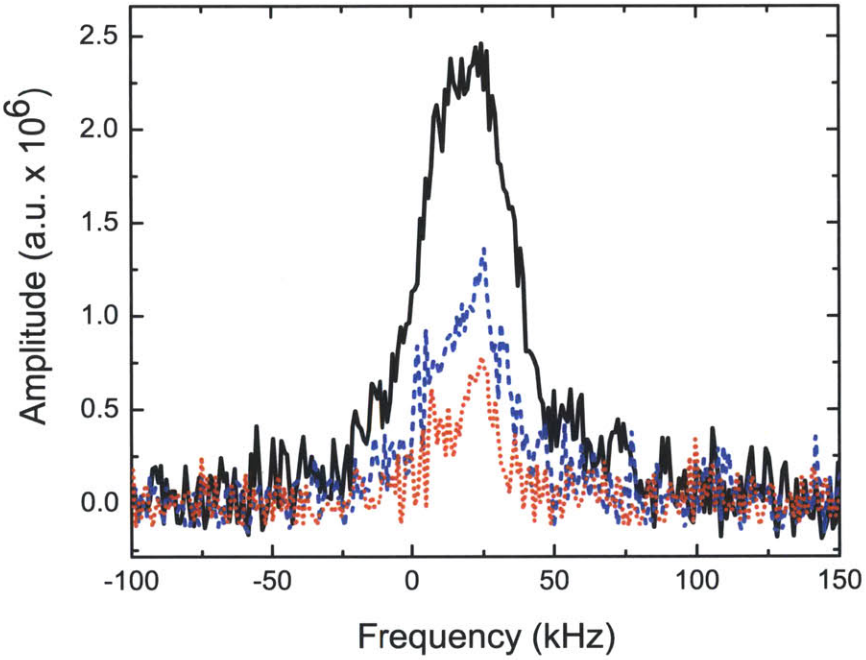

Figure 6-6: NMR spectra after 3s of DNP (red dotted curve), 7s (blue dashed), and 140s of DNP (black solid)

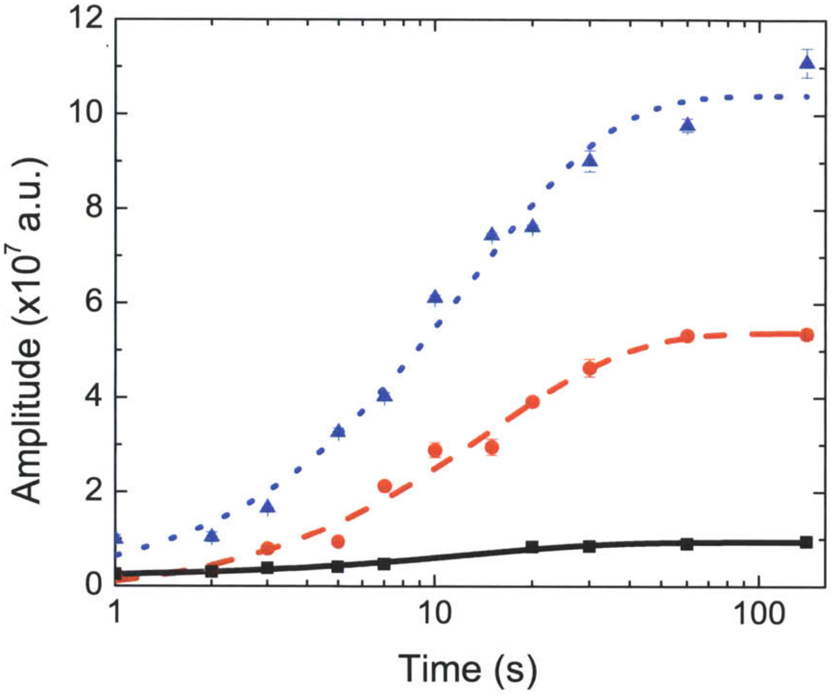

Figure 6-7: Results of the experimet with fits of the buildup curves. Blue triangles are the data from saturation with open system OCT pulses, red circles are for closed OCT pulses, and black squares are for hard pulses.

diffuse through the bulk. Thus we expect the effective T_1 of the bulk nuclear spins to be on the same order as the polarization buildup times, and in fact it is.

As mentioned in Chapter 3 saturating the electron spins cools not only the nuclear Zeeman bath but also the nuclear dipolar bath. Because the dipolar coupling is on the order of tens of kilohertz, the effective spin temperature after DNP can be μK. We measured the dipolar ordered states after DNP to compare to the Zeeman ordered states and to produce a more complete picture of the spin dynamics.

One standard method of measuring dipolar order is the Jeener-Broekaert echo. In this pulse sequence Zeeman order is converted to dipolar order, evolves for some time, and is then converted back to Zeeman order and read out as an echo. After DNP there is already polarization in the dipolar order, so we only need to apply a $\pi/4$ pulse to convert dipolar to Zeeman order and record the echo as the state evolves into an observable signal.

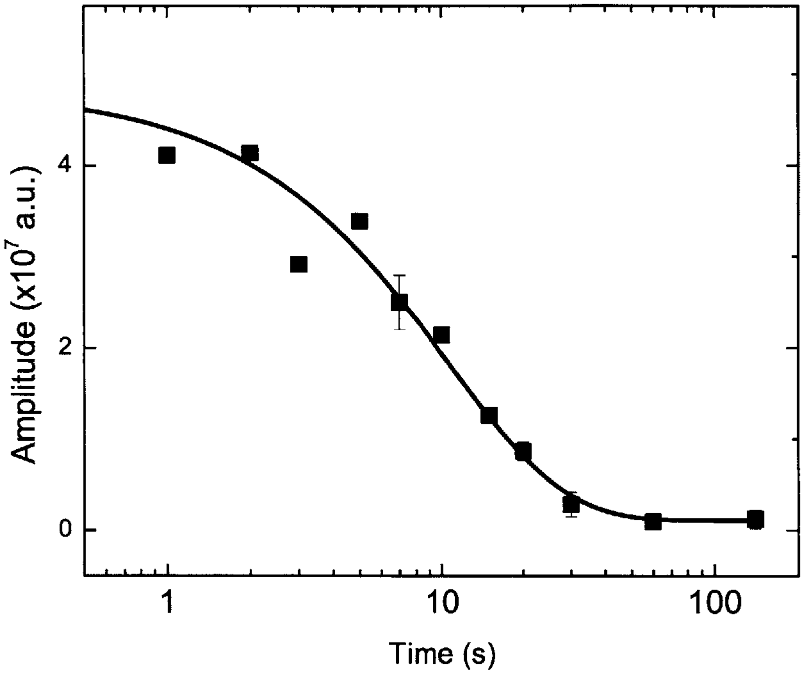

Figure 6-8: Effective T_1 measurement with fit.

The results of this measurement are shown in Fig 6-9. The final signal is 0.47 times that of the Zeeman ordered states. We expect that the dipolar order signal will at the most be half the amplitude of the Zeeman order because the detection uses a $\pi/4$ pulse in the measurement instead of a $\pi/2$, so only half of the magnetization is rotated into an observable.

The buildup time is 9.9 ± 1.8 s. While the enhancement of the dipolar signal matches expectations, the buildup time does not. The diffusion rate of dipolar order is typically an order of magnitude faster than Zeeman order diffusion for the reasons discussed in Chapter 1. It is possible that the detected signal is longitudinal order instead of dipolar; longitudinal order can be measured with the same scheme, but typically the amplitude is much smaller. Further experiments are needed to explain these results.

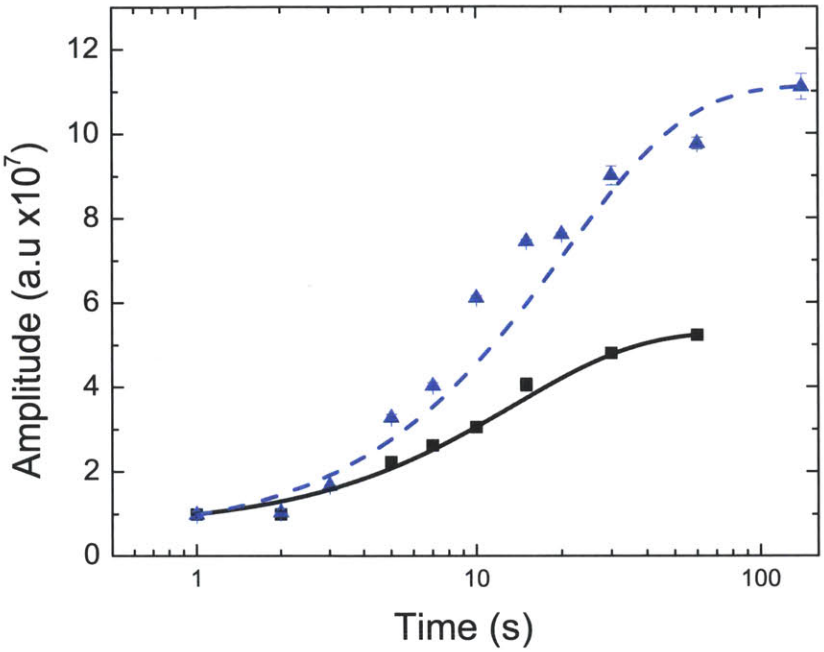

Figure 6-9: Dipolar order measurement: the dipolar order polarization is represented by the data with black squares, and is compared to Zeeman order polarization buildup is (blue triangles).

6.4 Analysis and Conclusions

These results clearly show that optimal control theory can improve polarization transfer in DNP experiments. Even with a relatively simple pulse sequence with few time steps we can achieve an order of magnitude increase in polarization using OCT pulses versus hard pulses. This is a significant signal enhancement, and a useful result within the field of DNP.

While the OCT pulses do produce a nuclear polarization enhancement of 180, this increase is less than the theoretical maximum enhancement of 660. The inability to reach this level of enhancement could be due to the unaccounted for leakage pathways or to asymmetric saturation of the electron resonances.

We imagine we can extend these results to find control sequences for larger spin systems. In particular we have neglected any nuclei further from the electron defect than the nearest proton. These nuclear spin may still have small hyperfine interactions with the electron spin, and we have not allowed any transfer pathways is the pulse optimization which might polarize these spins directly. We could also include the dipolar couplings between nuclear spins to simulate spin diffusion, the rate limiting step in this experiment.

It may also be useful to design control pulses for samples other than single crystals. In the case presented here the two spin system was assumed to be in the same orientation throughout the sample. DNP in powder samples would require optimizing pulses for a set of internal Hamiltonians. Such control is possible, but it is not know what additional resources would be needed.

More generally, this experiment demonstrates that we can design control sequences for open quantum systems that account for the interactions with the environment. Including relaxation processes in the pulse finder produces pulses that select the desired transitions more efficiently than using a superoperator that accounts only for unitary processes. This method of pulse finding is useful for quantum control in systems where relaxation plays a strong role in the dynamics. The Kraus operator description is particularly convenient as one can write a modular pulse finding code in which decoherent processes can be added to the superoperator successively.

Not only is it possible to create control operations in dissipative systems, but we have shown that an open quantum system approach can provide significant improvements over unitary control. We anticipate that superoperator optimized pulse design will lead to superior control in spin based systems and other quantum devices.

Chapter 7

Generating Noise Realizations

Often it is useful to simulate the results of a physical experiment, to predict the possible outcomes of the experiment or to understand the results according to a certain model. While there are many factors that can lead the experiment to deviate from the simulation, one reality of experiments is that every system will have noise. It is useful in many cases to characterize the noise itself. Simulating noisy processes, however, can be computationally intensive. There are several methods of producing colored noise functions [43], and in this chapter we present one method of generating realizations of noise belonging to a special, but highly useful, class of processes: Gaussian processes.

7.1 Gaussian Processes

A Gaussian process is, by definition, a process for which the value at every point in time is a random variable with a normal distribution. If one instance of the noise is $x_i(t)$, then over the set of instances i, each $x(t_j)$ has a normal distribution,

$$prob(x) = \frac{1}{\sigma\sqrt{2\pi}} exp(-(x-\mu)^2/2\sigma^2) \tag{7.1}$$

There are several properties which are characteristic of Gaussian processes [76]:

- Zero-mean: This first condition is not necessary for a Gaussian process, but we include it because we can remove any deviation from zero mean and describe the dynamics due to this offset with a Hamiltonian. The remaining stochastic process will be zero-mean, and by definition the ensemble average at each point in time will go to zero,

$$\langle x(t)\rangle = \lim_{N\to\infty} \frac{1}{N}\sum_{i=1}^{N} x_i(t) = 0 \tag{7.2}$$

- Stationarity: A process is stationary if the covariance between $x(t)$ at any two times depends only on the difference between the times. The covariance is given by the ensemble average of $x(t_1)$ and $x(t_2)$,

  $$G(t_1,t_2) = \langle x(t_1)x(t_2)\rangle = \lim_{N\to\infty} \frac{1}{N}\sum_{i=1}^{N} x_i(t_1)x_i(t_2) \tag{7.3}$$

  If $G(t_1,t_2)$ depends only on $\tau = (t_1 - t_2)$, then the process is stationary. Note that a stationary Gaussian process will also be ergodic, meaning the time average of $x_i(t)x_i(t+\tau)$ will converge to the ensemble average.

- Odd moments: All odd moments of a Gaussian process should go to zero [57](for example the third moment $\langle x(t_1)x(t_2)x(t_3)\rangle = 0$

- Even moments: The even moments should factor into products of the second moment [39, 57], i.e. for even n,

  $$\langle x(t_1)x(t_2)\ldots x(t_n)\rangle = \sum\prod x(t_i)x(t_j) \tag{7.4}$$

- Spectral Density: The spectral density function contains all the information about the noise process. This is not true in general, but it is valid for Gaussian processes. This is due to the relationship between the power spectral density and the autocorrelation function [14, 58, 5]. The power spectral density is defined as,

  $$S(\omega) = \lim_{T\to\infty} \frac{2\left\langle |X(w)|^2\right\rangle}{T} \tag{7.5}$$

  where $X(\omega)$ is the Fourier transform of the noise function $x(t)$. The autocorrelation function for a stationary and ergodic process is,

$$\phi_i(\tau) \equiv \overline{x_i(t)x_i(t+\tau)} = \lim_{T\to\infty} \frac{1}{T} \int_{-T/2}^{T/2} x_i(t)x_i(t+\tau)dt \tag{7.6}$$

$\phi(\tau)$ and $S(\omega)$ are a Fourier pair. To show this, we begin with the Parseval theorem,

$$\int_{-\infty}^{\infty} f(t)g^*(t)dt = \frac{1}{2\pi} \int_{-\infty}^{\infty} F(\omega)G^*(\omega)d\omega \tag{7.7}$$

where F and G are the Fourier transforms of f and g. It follows that,

$$\int_{-\infty}^{\infty} x(t)x(t+\tau)dt = \frac{1}{2\pi} \int_{-\infty}^{\infty} |X(\omega)|^2 e^{i\omega\tau} d\omega \tag{7.8}$$

We assume the noise function $x(t)$ is real-valued. Taking the ensemble and time averages of both sides of Eq. (7.8) we have

$$\lim_{T\to\infty} \frac{1}{T} \int_{-\infty}^{\infty} \langle x(t)x(t+\tau)\rangle \, dt = \lim_{T\to\infty} \frac{1}{2\pi} \int_{0}^{\infty} \frac{2\left\langle |X(\omega)|^2\right\rangle}{T} e^{i\omega\tau} d\omega \tag{7.9}$$

Finally we have,

$$\phi(\tau) = \frac{1}{2\pi} \int_{0}^{\infty} S(\omega) \cos{(\omega\tau)} d\omega \tag{7.10}$$

$$S(\omega) = 4 \int_{0}^{\infty} \phi(\tau) \cos{(\omega\tau)} d\tau \tag{7.11}$$

For a Gaussian process, if it is stationary and ergodic the covariance is equal to the autocorrelation function. Because the odd moments of such a process are zero, and the even moments are products of the two point correlation functions, if one knows the spectral density then one knows all the moments.

7.2 Algorithm

Here we present a method for generating noise realizations given a spectral density function. This method is known as 'phase randomization' and was first presented by

Yamada [96].

One often has access to the power spectrum of the noise in a physical system and can therefore characterize the noise with the power spectral density, $S(\omega)$. We assume that we have a known spectral density, $S(\omega)$, which is a real-valued and even function. Then we can generate instances of the noise function $n(t)$ by assigning a random phase to every point in $S(\omega)$, so $n(t)$ is

$$n(t) \equiv \int_{-\infty}^{\infty} \sqrt{S(\omega)} e^{i\phi(\omega)} e^{i\omega t} d\omega \tag{7.12}$$

$\phi(\omega)$ is a random variable with a uniform distribution. We ensure that $n(t)$ is also a real-valued function with the condition,

$$\phi(-\omega) = -\phi(\omega) \tag{7.13}$$

Note that this also forces the requirement $\phi(0) = 0$. Since $S(\omega)$ is even, we can write $n(t)$ as the cosine transform,

$$n(t) = 2\int_{0}^{\infty} \sqrt{S(\omega)} \cos(\omega t + \phi(\omega)) d\omega \tag{7.14}$$

The definition of the spectral density for an infinite process also includes the limit as the time T goes to infinity (Eq. 7.5). For finite processes, $n(t)$ should be equal to the Fourier transform in Eq. 7.12 multiplied by T. We will assume for simplicity that this scaling factor is absorbed in the spectral density function for the following analysis.

Now we will show that $n(t)$ satisfies the conditions for a Gaussian process given in the previous section.

- Zero-mean: We have to show that $\langle n(t) \rangle = 0$.

$$\begin{aligned} \langle n(t) \rangle &= 2\int_{0}^{\infty} \sqrt{S}(\omega) \left\langle \cos(\omega t + \phi(\omega)) \right\rangle d\omega & (7.15) \\ &= \int_{0}^{\infty} \sqrt{S(\omega)} \left[\cos(\omega t) \left\langle \cos(\phi(\omega)) \right\rangle - \sin(\omega t) \left\langle \sin(\phi(\omega)) \right\rangle \right] d\omega & (7.16) \end{aligned}$$

Given that $\phi(\omega)$ is uniformly distributed on the interval $[0, 2\pi]$, the averages $\langle\cos(\omega)\rangle$ and $\langle\sin(\omega)\rangle$ are zero. Thus the ensemble average of $n(t)$ is zero.

- Stationary: Now we show that the covariance, $G(t_1, t_2)$, depends only on the difference, $(t_1 - t_2)$.

$$\begin{aligned} G(t_1, t_2) &= \langle n(t_1) n(t_2)\rangle \qquad (7.17)\\ &= 4\int_0^\infty \int_0^\infty \sqrt{S(\omega_1)S(\omega_2)} \\ &\qquad \times \langle\cos(\omega_1 t_1 + \phi(\omega_1))\cos(\omega_2 t_2 + \phi(\omega_2))\rangle\, d\omega_1 d\omega_2 \qquad (7.18)\end{aligned}$$

The cosine terms here can be expanded using trig identities to

$$\begin{aligned} &\langle\cos(\omega_1 t_1 + \phi(\omega_1))\cos(\omega_2 t_2 + \phi(\omega_2))\rangle = \\ &\frac{1}{2}\langle\cos(\omega_1 t_1 + \omega_2 t_2)\cos(\phi(\omega_1) + \phi(\omega_2)) + \cos(\omega_1 t_1 - \omega_2 t_2)\cos(\phi(\omega_1) - \phi(\omega_2)) \\ &- \sin(\omega_1 t_1 + \omega_2 t_2)\sin(\phi(\omega_1) + \phi(\omega_2)) - \sin(\omega_1 t_1 - \omega_2 t_2)\sin(\phi(\omega_1) - \phi(\omega_2))\rangle \\ &\qquad (7.19)\end{aligned}$$

$\phi(\omega_1)$ and $\phi(\omega_2)$ are independent random variables, so the ensemble average is essentially and ensemble average with respect to $\phi(\omega_1)$ and then with respect to $\phi(\omega_2)$, ie

$$\begin{aligned} &\langle\cos(\omega_1 t_1 + \phi(\omega_1))\cos(\omega_2 t_2 + \phi(\omega_2))\rangle = \\ &\qquad \langle\langle\cos(\omega_1 t_1 + \phi(\omega_1))\cos(\omega_2 t_2 + \phi(\omega_2))\rangle_1\rangle_2 = 0 \qquad (7.20)\end{aligned}$$

and similar for the sine terms. When $\omega_1 \neq \omega_2$, the ensemble average in Eq. (7.19) is zero. When $\omega_1 = \omega_2$, however, we have $\langle\cos(\omega_1 t_1 + \phi(\omega_1))\cos(\omega_2 t_2 + \phi(\omega_2))\rangle = 1$. Thus the ensemble average gives us a delta function in the integral in Eq.

(7.18), and the only term from Eq. (7.19) is $\cos(\omega_1 t_1 - \omega_2 t_2)$,

$$
\begin{aligned}
G(t_1, t_2) &= 2\int_0^\infty \int_0^\infty \sqrt{S(\omega_1)S(\omega_2)} cos(\omega_1 t_1 - \omega_2 t_2)\delta(\omega_1 - \omega_2) d\omega_1 d\omega_2 \\
&= 2\int_0^\infty S(\omega_1)\cos(\omega_1(t_1 - t_2))d\omega_1 \qquad (7.21)
\end{aligned}
$$

$G(t_1, t_2)$ depends only on $(t_1 - t_2)$, so $n(t)$ is stationary.

- Odd Moments: Similarly we find that the odd moments are all zero. The product of three cosine terms in the integral of $\langle n(t_1)n(t_2)(t_3)\rangle$ can be expanded to,

$$
\begin{aligned}
&\frac{1}{4}\langle \cos(\omega_1 t_1 + \omega_2 t_2 + \omega_3 t_3)\cos(\phi(\omega_1) + \phi(\omega_2) + \phi(\omega_3)) \\
&\quad + \cos(\omega_1 t_1 - \omega_2 t_2 - \omega_3 t_3)\cos(\phi(\omega_1) - \phi(\omega_2) - \phi(\omega_3)) \\
&\quad + \cos(\omega_1 t_1 + \omega_2 t_2 - \omega_3 t_3)\cos(\phi(\omega_1) + \phi(\omega_2) - \phi(\omega_3)) \\
&\quad + \cos(\omega_1 t_1 - \omega_2 t_2 + \omega_3 t_3)\cos(\phi(\omega_1) - \phi(\omega_2) + \phi(\omega_3)) \\
&\quad + \ (\text{sine terms})\rangle \qquad (7.22)
\end{aligned}
$$

As in the lower order moments, the sine terms always average to zero, and the cosine terms average to zero when the arguments do not equal to zero. While it is possible for certain values of $\{\omega_1, \omega_2, \omega_3\}$ that one of the cosine terms, say $\cos(\phi(\omega_1) - \phi(\omega_2) - \phi(\omega_3))$, equals one, this will not happen on average over many realizations. There is no condition here to produce a delta function, and the third moment is always zero. This will be true for all odd moments.

- Even Moments: The final requirement on the moments of $n(t)$ is that the even moments factor into products of the second moment. The ensemble average in $\langle n(t_1)n(t_2)n(t_3)n(t_4)\rangle$ yields the following terms,

$$
\begin{aligned}
&\frac{1}{8}\langle \cos(\omega_1 t_1 + \omega_2 t_2 + \omega_3 t_3 + \omega_4 t_4)\cos(\phi(\omega_1) + \phi(\omega_2) + \phi(\omega_3) + \phi(\omega_4)) \\
&\quad + \cos(\omega_1 t_1 - \omega_2 t_2 - \omega_3 t_3 - \omega_4 t_4)\cos(\phi(\omega_1) - \phi(\omega_2) - \phi(\omega_3) - \phi(\omega_4))
\end{aligned}
$$

$$
\begin{aligned}
&+\cos(\omega_1 t_1 - \omega_2 t_2 + \omega_3 t_3 - \omega_4 t_4)\cos(\phi(\omega_1) - \phi(\omega_2) + \phi(\omega_3) - \phi(\omega_4))\\
&+\cos(\omega_1 t_1 + \omega_2 t_2 + \omega_3 t_3 - \omega_4 t_4)\cos(\phi(\omega_1) + \phi(\omega_2) + \phi(\omega_3) - \phi(\omega_4))\\
&+\cos(\omega_1 t_1 + \omega_2 t_2 - \omega_3 t_3 - \omega_4 t_4)\cos(\phi(\omega_1) + \phi(\omega_2) - \phi(\omega_3) - \phi(\omega_4))\\
&+\cos(\omega_1 t_1 - \omega_2 t_2 - \omega_3 t_3 + \omega_4 t_4)\cos(\phi(\omega_1) - \phi(\omega_2) - \phi(\omega_3) + \phi(\omega_4))\\
&+\cos(\omega_1 t_1 + \omega_2 t_2 - \omega_3 t_3 + \omega_4 t_4)\cos(\phi(\omega_1) + \phi(\omega_2) - \phi(\omega_3) + \phi(\omega_4))\\
&+\cos(\omega_1 t_1 - \omega_2 t_2 + \omega_3 t_3 + \omega_4 t_4)\cos(\phi(\omega_1) - \phi(\omega_2) + \phi(\omega_3) + \phi(\omega_4))\\
&+\ \text{(sine terms)}\ \rangle
\end{aligned}
\tag{7.23}
$$

There are three terms in Eq. (7.23) which can produce non-zero contributions to the ensemble average with certain conditions on the ω_i. For example, $\cos(\phi(\omega_1) - \phi(\omega_2) + \phi(\omega_3) - \phi(\omega_4)) = 1$ when $\omega_1 = \omega_2$ and $\omega_3 = \omega_4$, or $\omega_1 = \omega_4$ and $\omega_2 = \omega_3$. Eq. (7.23) yields three sets of delta functions:

$$
\begin{aligned}
&\cos(\phi(\omega_1) - \phi(\omega_2) + \phi(\omega_3) - \phi(\omega_4)) \Rightarrow \delta(\omega_1 - \omega_2)\delta(\omega_3 - \omega_4) + \delta(\omega_1 - \omega_4)\delta(\omega_2 - \omega_3)\\
&\cos(\phi(\omega_1) + \phi(\omega_2) - \phi(\omega_3) - \phi(\omega_4)) \Rightarrow \delta(\omega_1 - \omega_3)\delta(\omega_2 - \omega_4) + \delta(\omega_1 - \omega_4)\delta(\omega_2 - \omega_3)\\
&\cos(\phi(\omega_1) - \phi(\omega_2) - \phi(\omega_3) + \phi(\omega_4)) \Rightarrow \delta(\omega_1 - \omega_2)\delta(\omega_3 - \omega_4) + \delta(\omega_1 - \omega_3)\delta(\omega_2 - \omega_4)
\end{aligned}
\tag{7.24}
$$

Integrating over these delta functions gives

$$
\langle n(t_1)n(t_2)n(t_3)n(t_4)\rangle = \tag{7.25}
$$

$$
\begin{aligned}
&16 \times \frac{1}{8}\left[\int_0^\infty\int_0^\infty S(\omega_2)S(\omega_4)\cos(\omega_2(t_1 - t_2)\cos(\omega_4(t_3 - t_4))d\omega_2 d\omega_4\right.\\
&\left. + \int_0^\infty\int_0^\infty S(\omega_4)S(\omega_3)\cos(\omega_4(t_1 - t_4)\cos(\omega_3(t_2 - t_3))d\omega_3 d\omega_4 + \text{ etc.}\right]\\
&= \langle n(t_1)n(t_2)\rangle\langle n(t_3)n(t_4)\rangle + \langle n(t_1)n(t_3)\rangle\langle n(t_2)n(t_4)\rangle + \langle n(t_1)n(t_4)\rangle\langle n(t_2)n(t_3)\rangle
\end{aligned}
\tag{7.26}
$$

For all the even moments, the only terms that will contribute will be those that produce products of delta functions. The final integral will reduce to produces of the second moment.

- Spectral Density:

- $S(\omega)$: There is one subtlety to complicate the above analysis - the case when $S(0) \neq 0$. Because $\phi(0) = 0$ for every instance of $n(t)$, there is a nonzero DC contribution to the noise function, and the mean is nonzero:

  $$\langle n(t) \rangle = 2 \int_0^\infty \sqrt{S(\omega)} \delta(\omega) d\omega = 2\sqrt{S(0)} \tag{7.27}$$

  Additionally, the higher order moments have extra terms, so the odd moments are also nonzero and the even moments contain an extra constant. The simple solution is to subtract the DC componenet off from $n(t)$ in Eq. (7.14),

  $$n(t) \equiv 2 \int_0^\infty \sqrt{S(\omega)} \cos(\omega t + \phi(\omega)) d\omega - 2\sqrt{S(0)} \tag{7.28}$$

  Now $n(t)$ is zero mean, and the higher order moments are likewise corrected.

This algorithm produces noise instances from a spectral density function that satisfy the conditions for a stochastic Gaussian process. The method presented here is not computationally intensive, as it depends mainly on taking the Fourier transform in Eq. 7.14. After generating many noise functions, we can also compare the correlation matrix of the ensemble average, C of these functions to the correlation matrix determined by the spectral density, C_S. We propose the one norm,

$$||C_S - C||_1 = ||M||_1 = \max_j \left(\sum_i M_{ij} \right) \tag{7.29}$$

as a metric for assessing the quality of the generated noise.

7.3 An Example

We present a numerical demonstration of the algorithm. The spectral density of the noise to be generated in this example is a Lorentzian with a correlation time τ_c (Fig.

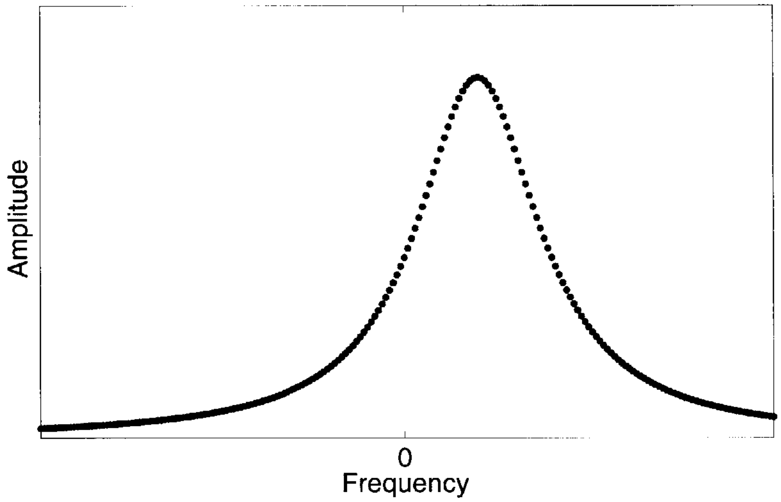

Figure 7-1: Lorentzian spectral density function (arbitrary units).

7-1),

$$S(\omega) = \frac{2(A^2/\tau_c)}{(\omega - \omega_0)^2 + (1/\tau_c^2)}$$

We generate an instance of the noise, n points long, using the random phase assignment, and repeat this process N times to create an ensemble of noise instances. Fig. 7-2 shows one instances of the noise generated.

We calculated the covariance matrix for the ensemble of noise functions and ideal covariance matrix determined by the spectral density. The ideal covariance matrix is constructed by first taking the Fourier transform of the spectral density $S(\omega)$ to find the covariance function $G(\tau)$. The matrix elements of C_S are defined as

$$C_S(i,j) = G(i-j)$$

This matrix will have constant diagonals.

If $n(t)$ represents the ensemble of noise functions, the covariance matrix of the noise functions the elements $C(i,j)$ are the covariances,

$$C(i,j) = \langle n(t_i) n(t_j) \rangle$$

For the Lorentzian spectral density, Fig. 7-3 shows the decrease in the one-norm,

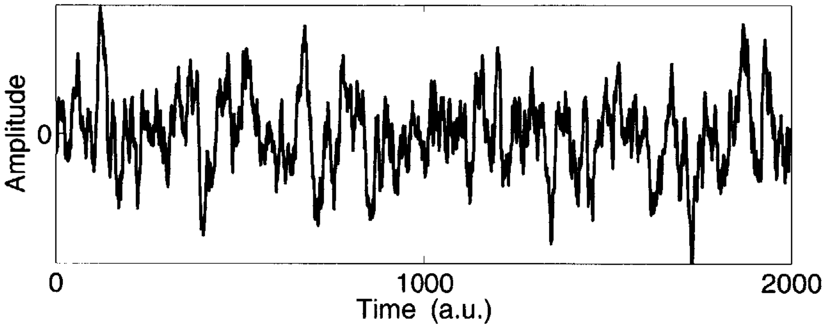

Figure 7-2: One instances of the noise generated from the Lorentzian spectral density.

$||C_S - C||_1$, as we increase the number of generated noise functions. The smaller this metric is, the closer the generated noise is to stochastic noise with the correct spectral density. We see from this figure that the norm converges quickly to a value of 2×10^{-4}, and according to fits of this data, this convergence is faster than $\sqrt{N}$ where N is the number of noise instances.

7.4 Conclusions

Overall this algorithm is a simple and direct means of producing instances of noise using minimal computational effort. This method of generating instances of a process with a given spectral density is also known as 'surrogate data' [72] or 'Fourier bootstrapping' [13], but we believe this to be a novel application of the method for the purpose of generating noise. The ability to quickly and reliably produce noise functions will allow for accurate design and simulations of control sequences in systems where the noise spectral density is known. As quantum control techniques become more refined, it is becoming increasingly necessary to account for all system dynamics including interactions with the environment and stochastic noise processes.

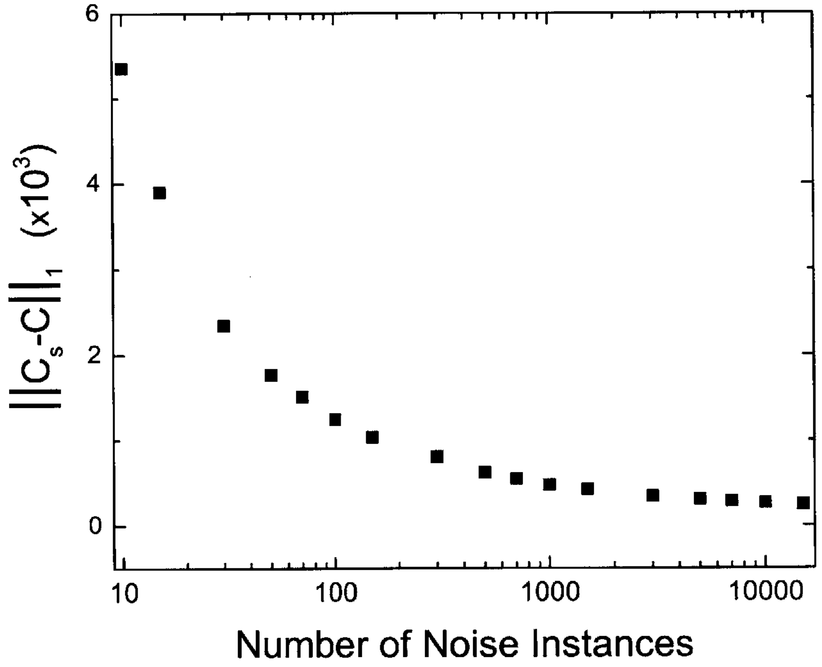

Figure 7-3: Convergence of the one norm between the ideal and actual covariance matrices as a function of the number of instances generated.

Bibliography

[1] Nmr quantum information processing. *Experimental Aspects of Quantum Computing*, pages 15–44, 2005.

[2] A. Abragam. *Principles of Magnetic Resonance.* Oxford University Press, Oxford, UK, 1961.

[3] A. Abragam and M. Goldman. Principles of dynamic nuclear polarisation. *Reports on Progress in Physics*, 41(3), 1978.

[4] R. Alicki and K. Lendi. Quantum dynamical semigroups and applications. *Lecture Notes in Physics*, 717, 2007.

[5] A. Ambrozy. *Electronic Noise.* McGraw-Hill, New York, 1982.

[6] J. W. Aptekar, M.C. Cassidy, A. C. Johnson, R.A. Barton, M. Lee, A.C. Ogier, C. Vo, M. N. Anahtar, Y. Ren, S. N. Bhatia, C. Ramanathan, D.G. Cory, A.L. Hill, R.W. Mair, M.S. Rosen, R.L. Walsworth, and C.M. Marcus. Silicon nanoparticles as hyperpolarized magnetic resonance imaging agents. *ACS Nano*, 3(12):4003–4008, 2009.

[7] J. Baugh, O. Moussa, C.A. Ryan, R. Laflamme, C. Ramanathan, T.F. Havel, and D.G. Cory. Solid-state nmr three-qubit homonuclear system for quantum-information processing: Control and characterization. *Phys. Rev. A*, 73:022305, 2006.

[8] N. Bloembergen. On the interaction of nuclear spins in a crystalline lattice. *Physica*, 15:386–426, 1949.

[9] N. Bloembergen, E.M. Purcell, and R.V. Pound. Relaxation effects in nuclear magnetic resonance absorption. *Physical Review*, 73:679–746, 1948.

[10] T.W. Borneman and D.G. Cory. Bandwidth-limited control and ringdown suppression in high-q resonators. *Journal of Magnetic Resonance*, 225:120–129, 2012.

[11] T.W. Borneman, M.D. Hurlimann, and D.G. Cory. Application of optimal control to cpmg refocusing pulse design. *Journal of Magnetic Resonance*, 207:220–223, 2010.

[12] G.S. Boutis, D. Greenbaum, H. Cho, D.G. Cory, and C. Ramanathan. Spin diffusion of correlated two-spin states in a dielectric crystal. *Physical Review Letters*, 92:137201, 2004.

[13] W.J. Braun and R.J. Kulperger. Properties of a fourier bootstrap method for time series. *Communications in Statistics - Theory and Methods*, 26:1329–1336, 1998.

[14] M.J. Buckingham. *Noise in Electronic Devices and Systems.* Ellis Horwood Pub., 1983.

[15] P. Cappellaro, J. Emerson, N. Boulant, C. Ramanathan, S. Lloyd, and D.G. Cory. Entanglement assisted metrology. *Physical Review Letters*, 94:020502, 2005.

[16] T.T. Carver and C.P. Slichter. Experimental verification of the overhauser nuclear polarization effect. *Physical Review*, 102:975–980, 1956.

[17] J. Cavanagh, W.J. Fairbrother, A.G. III Palmer, N.J. Skelton, and M. Rance. *Protein NMR Spectroscopy: Principles and Practice.* Academic Press, Burlington,MA, 2007.

[18] H.J. Cho, J. Baugh, C.A. Ryan, D.G. Cory, and Ramanathan. Low temperature probe for dynamic nuclear polarization and multiple-pulse solid-state nmr. *Journal of Magnetic Resonance*, 187:242–250, 2007.

[19] M.-D. Choi. Completely positive linear maps on complex matrices. *Linear Algebra andIts Applications*, 10:285–290, 1975.

[20] I.L. Chuang, N. Gershenfeld, and M. Kubinec. Experimental implementation of fast quantum searching. *Phys. Rev. Lett.*, 80:3408–3411, 1998.

[21] A. Comment, J. Rentsch, F. Kurdzesau, S. Jannin, K. Uffmann, R.B. van Heeswijk, P. Hautle, J.A. Konter, B. van den Brandt, and van der Klink J.J. Producing over 100 ml of highly concentrated hyperpolarized solution by means of dissolution dnp. *Journal of Magnetic Resonance*, 104, 2008.

[22] D. G. Cory, M. D. Price, W. Maas, E. Knill, R. Laflamme, W. H. Zurek, T. F. Havel, and S. S. Somaroo. Experimental quantum error correction. *Phys. Rev. Lett.*, 81:2152–2155, 1998.

[23] D.G. Cory, A.F. Fahmy, and T.F. Havel. Ensemble quantum computing by nmr spectroscopy. *Proceedings of the National Academy of Sciences*, 95:1634–1639, 1997.

[24] B. Corzilius, A.A¿ Smith, and R.G. Griffin. Solid effect in magic angle spinning dynamic nuclear polarization. *Journal of Chemical Physics*, 137:054201, 2012.

[25] L.R. Dalton, A. Bain, and C.L. Young. Recent advances in electron paramagnetic resonance. *Ann. Rev. Phys. Chem.*, 41:389–407, 1990.

[26] L.R. Dalton, A.L. Kwiram, and J.A. Cowen. Electron spin-lattice and cross relaxation in irradiated malonic acid. *Chemical Physics Letters*, 14(1):77–81, 1971.

[27] P. Doria, T. Calarco, and S. Montangero. Optimal control technique for many-body quantum dynamics. *Physical Review Letters*, 106:190501, 2011.

[28] G.R. Eaton and S.S. Eaton. *Foundations of Modern EPR.* World Scientific Publishing Co. Pte. Ltd., River Edge, NJ, 1997.

[29] J. Forrer, S. Pfenniger, J. Eisenegger, and A. Schweiger. A pulsed endor probehead with the bridged loop gap resonator: Construction and performance. *Review of Scientific Instruments*, 61:3360, 1990.

[30] E.M. Fortunato, M.A. Pravia, N. Boulant, G. Teklemariam, T.F. Havel, and D.G. Cory. Design of strongly modulating pulses to implement precise effective hamiltonians for quantum information processing. *Journal of Chemical Physics*, 116(17):7599–7606, 2002.

[31] J.A. Goedkoop and C.H. MacGillavry. The crystal structure of malonic acid. *Acta Crystallographica*, 10:125–127, 1957.

[32] D. Greenbaum, M. Kindermann, C. Ramanathan, and D.G. Cory. A hydrodynamic approach to coherent nuclear-spin transport. *Physical Review B*, 71, 2005.

[33] Daniel Greenbaum. *Quantum Spin Transport in Paramagnetic Systems.* PhD thesis, Massachusetts Institute of Technology, 2005.

[34] T. Havel. Robust procedures for converting among lindblad, kraus and matrix representations of quantum dynamical semigroups. *Journal of Mathematical Physics*, 44(2):534–557, 2003.

[35] F.W. Hersman, I.C. Ruset, S. Ketel, I. Muradian, S.D. Covrig, J. Distelbrink, W. Porter, D. Watt, J. Ketel, J. Brackett, A. Hope, and S. Patz. Large production system for hyperpolarized 129xe for human lung studies. *Academic radiology*, 15:683–292, 2008.

[36] J. Hodges, J.C. Yang, C. Ramanathan, and D.G. Cory. Universal control of nuclear spins via anisotropic hyperfine interactions. *Physical Review A*, 78, 2008.

[37] Y. Hovav, A. Feintuch, and S. Vega. Dynamic nuclear polarization assisted spin diffusion for the solid effect case. *Journal of Chemical Physics*, 134(074509), 2011.

[38] K.-N. Hu, C. Song, H.-H. Yu, T.M. Swager, and R.G. Griffin. High-frequency dynamic nuclear polarization using biradicals: A multifrequency epr lineshape analysis. *Journal of Chemical Physics*, 128:052302, 2008.

[39] L. Isserlis. On a formula for the product-moment coefficient of an order of a normal frequency distribution in an number of variables. *Biometrika*, 12:134–139, 1918.

[40] C.D. Jeffries. *Dynamic Nuclear Orientation.* Interscience, 1932.

[41] J.A. Jones, M. Mosca, and R.H. Hansen. Implementation of a quantum search algorithm on a quantum computer. *Nature*, 393:344–346, 1998.

[42] B.E. Kane. A silicon-based nuclear spin quantum computer. *Nature*, 393:133–137, 1998.

[43] N.J. Kasdin. Discrete simulation of colored noise and stochastic processes and $1/f^{\alpha}$ power law noise generation. *Proceedings of the IEEE*, 83(5), 1995.

[44] N. Khaneja, R. Brockett, and S.J. Glaser. Time optimal control in spin systems. *Physical Review A*, 63(032308), 2001.

[45] N. Khaneja, T. Reiss, C. Kehlet, T. Schulte-Herbruggen, and S.J. Glaser. Optimal control of coupled spin dynamics: design of nmr pulse sequences by gradient ascent algorithms. *Journal of Magnetic Resonance*, 172:296–305, 2005.

[46] K. Kraus. General state changes in quantum theory. *Annals of Physics*, 64:311–335, 1971.

[47] K. Kraus. *States, Effects and Operations.* Springer-Verlag, Berlin, 1983.

[48] T. D. Ladd, J. R. Goldman, F. Yamaguchi, Y. Yamamoto, E. Abe, and K. M. Itoh. All-silicon quantum computer. *Phys. Rev. Lett.*, 89:017901, 2002.

[49] D.W. Leung. Choi's proof and quantum process tomography. *J. Math. Phys.*, 44:528–533, 2003.

[50] G. Lindblad. On the generators of quantum dynamical semigroups. *Communications in Mathematical Physics*, 48:119–130, 1976.

[51] N. Linden, H. Barjat, and R. Freeman. An implementation of the deutschjozsa algorithm on a three-qubit nmr quantum computer. *Chemical Physics Letters*, 296:61 – 67, 1998.

[52] L.L. Lumata, M.E. Merritt, C.R. Malloy, A.D. Sherry, J. van Tol, L. Song, and Z. Kovacs. Dissolution dnp-nmr spectroscopy using galvinoxyl as a polarizing agent. *Journal of Magnetic Resonance*, 227:14–19, 2013.

[53] A. Lund. *Principles and Applications of ESR Spectroscopy.* Springer Netherlands, 2011.

[54] S. Machnes, U. Sander, S.J. Glaser, P. de Fouquieres, A. Gruslys, S. Schirmer, and T. Schulte-Herbruggen. Comparing, optimizing, and benchmarking quantum-control algorithms in a unifying programming framework. *Physical Review A*, 84:022305, 2011.

[55] T. Maly, G.G. Debelouchina, V.S. Bajaj, K.-N. Hu, C.-G. Joo, M.L. Mak-Jurkauskas, J.R. Sirigiri, P.C.A. van der Wel, J. Herzfeld, R.J. Temkin, and R.G. Griffin. Dynamic nuclear polarization at high magnetic fields. *Journal of Chemical Physics*, 128:052211, 2008.

[56] I.I. Maximov, Z. Tosner, and N.C. Nielsen. Optimal control design of nmr and dynamic nuclear polarization experiments using monotonically convergent algorithms. *Journal of Chemical Physics*, 128:184505, 2008.

[57] J.V. Michalowicz, J.M. Nichols, F. Bucholtz, and C.C. Olson. An isserlis' theorem for mixed gaussian variables: application to the auto-bispectral density. *Journal of Statistical Physics*, 136:89–102, 2009.

[58] D.F. Mix. *Random Signal Processing.* Prentice Hall, Englewood Cliffs, 1995.

[59] K.W. Moore and H. Rabitz. Exploring quantum control landscapes: Topology, features, and optimization scaling. *Physical Review A*, 84, 2011.

[60] L.T. Muus, P.W. Atkins, and K.A. McLauchlan. *Chemically Induced Magnetic Polarisation.* D. Reidel, Dordrecht, 1977.

[61] J. Natterer and J. Bargon. Parahydrogen induced polarization. *Progress in Nuclear Magnetic Resonance Spectroscopy*, 31:293–315, 1997.

[62] C. Negrevergne, T.S. Mahesh, C.A. Ryan, M. Ditty, F. Cyr-Racine, W. Power, N. Boulant, T. Havel, D.G. Cory, and R. Laflamme. Benchmarking quantum control methods on a 12-qubit system. *Physical Review Letters*, 96:170501, 2006.

[63] J.A. Nelder and R. Mead. A simplex method for function minimization. *The Computer Journal*, 7:308–313, 1965.

[64] M.A. Nielsen. A simple formula for the average gate fidelity of a quantum dynamical operation. *Physics Letters A*, 303:249–252, 2002.

[65] M.A. Nielsen and I.L. Chuang. *Quantum Computation and Quantum Information.* Cambridge University Press, 2000.

[66] A.W. Overhauser. Polarization of nuclei in metals. *Physical Review*, 92:411–415, 1953.

[67] A. Oza, A. Pechen, J. Dominy, V. Beltrani, K. Moore, and H Rabitz. Optimization search effor over the control landscapes for open quantum systems with kraus-map evolution. *Journal of Physics A*, 42:205305, 2009.

[68] S. Pfenniger, J. Forrer, and Th. Weiland. Bridged loop-gap resonator: A resonant structure for pulsed esr transparent to highfrequency radiation. *Rev. Sci. Instrum*, 59:752, 1988.

[69] W. Plasecki and W. Francisz. Field distributions in loop-gap resonators. *Meas. Sci. Technol.*, 4:1363–1369, 1993.

[70] M.A. Pravia, N. Boulant, J. Emerson, A. Farid, E.M Fortunato, T.F. Havel, R. Martinez, and D.G. Cory. Robust control of quantum information. *Journal of Chemical Physics*, 119(19), 2003.

[71] J. Preskill. Lecture notes for physics 229: Quantum information and computation, 1998.

[72] D. Prichard and J. Theiler. Generating surrogate data for time series with several simultaneously measured variables. *Physical Review Letters*, 73:951–954, 1994.

[73] T.F. Prisner. *Dynamic Nuclear Polarization, in NMR Biomolecules: Towards Mechanistic Systems Biology.* Wiley-VCH Verlag, Weinheim, Germany, 2012.

[74] H.A. Rabitz, M.M. Hsieh, and C.M. Rosenthal. Quantum optimally controlled transition landscapes. *Science*, 303(5666):1998–2001, 2004.

[75] C. Ramanathan. Dynamic nuclear polarization and spin diffusion in nonconducting solids. *Applied Magnetic Resonance*, 34:409–421, 2008.

[76] C.E. Rasmussen and C.K.I. Williams. *Gaussian Processes for Machine Learning.* MIT Press, 2006.

[77] P.H. Reiger. *Electron Spin Resonance: Analysis and Interpretation.* Royal Society of Chemistry, Cambridge, UK, 2007.

[78] G.A. Rinard and G.R. Eaton. Loop-gap resonators. *Biological Magnetic Resonance*, 24B:19–52, 2005.

[79] C.A. Ryan, C. Negrevergne, M. Laforest, E. Knill, and R. Laflamme. Liquid-state nuclear magnetic resonance as a testbed for developing quantum control methods. *Physical Review A*, 78(012328), 2008.

[80] E. Sagstuen, A. Lund, Y. Itagaki, and J. Maruani. Weakly coupled proton interactions in the malonic acid radical: Single crystal endo analysis and epr simulation at microwave saturation. *J. Phys. Chem. A*, 104:6362–6371, 2000.

[81] J.J. Shane, I. Gromov, S. Vega, and D. Goldfarb. A versatile pulsed x-band endor spectrometer. *Review of Scientific Instruments*, 69:3357–3364, 1998.

[82] C.P. Slichter. *Principles of Magnetic Resonance.* Springer-Verlag, New York, 1990.

[83] I. Solomon. Relaxation processes in a system of two spins. *Physical Review*, (2):559–565, 1955.

[84] M. Steger, K. Saeedi, M.L.W. Thewalt, J.J.L. Morton, H. Riemann, N.V. Abrosimov, P. Becker, and H.-J. Pohl. Quantum information storage for over 180s using donor spins in a 28si "semiconductor vacuum". *Science*, 336(6086):1280–1283, 2012.

[85] G. Sturm, A. Lotz, and J. Voitlander. Pulsed epr with field cycling and a bridged loop-gap resonator made by chemical deposition of silver. *Journal of Magnetic Resonance*, 127:105–108, 1997.

[86] K. Suchanek, K. Cieslar, Z. Olejniczak, T. Palasz, M. Suchanek, and T. Dohnalik. Hyperpolarized gas imaging of the lung. *Optica Applicata*, 35:263–276, 2005.

[87] D. Suter and K. Lim. Scalable architecture for spin-based quantum computers with a single type of gate. *Physical Review A*, 65:052309, 2002.

[88] D. Suter and T.S. Mahest. Spins as qubits: Quantum information processing by nuclear magnetic resonance. *Vir. J. Nan. Sci. Tech.*, 128:052206, 2008.

[89] K. H. Sze, Q. Wu, H.S. Tse, and G. Zhu. Dynamic nuclear polarization: New methodology and applications. *Topics in Current Chemistry*, 326:215–242, 2012.

[90] K.R. Thurber, A. Potapov, W.M. Yau, and R. Tycko. Solid state nuclear magnetic resonance with magic-angle spinning and dynamic nuclear polarization below 25k. *Journal of Magnetic Resonance*, 226:100–6, 2013.

[91] E.J.R. van Beek, J.M. Wild, H.U. Kauczor, W. Schreiber, J.P. Mugler, and E.E. de Lange. Function mri of the lung using hyperpolarized 3-helium gas. *Journal of Magnetic Resonance Imaging*, 20:540–554, 2004.

[92] M.S. Vinding, I.I. Maximov, Z. Tosner, and N Nielsen. Fast numerical design of spatial-selective rf pulses in mri using krotov and quasi-newton based optimal control methods. *Journal of Chemical Physics*, 137:054203, 2012.

[93] Y.S. Weinstein, T.H. Havel, J. Emerson, and N. Boulant. Quantum process tomography of the quantum fourier transform. *Journal of CHemical Physics*, 121:6117–6133, 2004.

[94] V. Weis, M. Bennati, M. Rosay, J.A. Bryant, and R.G. Griffin. High-field dnp and endor with a novel multiple-frequency resonance structure. *Journal of Magnetic Resonance*, 140:293–299, 1999.

[95] R.A. Wind, M.J. Duijvestijn, C. van der Lugt, A. Manenschijn, and J. Vriend. Application of dynamic nuclear polarization in 13-c nmr in solids. *Progress in NMR Spectroscopy*, 17:33–67, 1985.

[96] M. Yamada and K. Ohkitani. Orthonormal wavelet analysis of turbulence. *Fluid Dynamics Research*, 8:101–115, 1991.